

POLISH ACADEMY OF SCIENCES – WROCLAW BRANCH

WROCLAW UNIVERSITY OF TECHNOLOGY

ARCHIVES OF CIVIL AND MECHANICAL ENGINEERING

**Quarterly
Vol. IV, No. 4**

WROCLAW 2004

Cross-current lamella sedimentation tanks

WŁODZIMIERZ P. KOWALSKI, RAFAŁ MIĘSO

University of Mining and Metallurgy, Al. Mickiewicza 30, Kraków

The paper outlines the design of sedimentation tanks and installations utilising the Boycott's effect. Three major types of configuration of lamella installations are presented: counter-current, cross-current and parallel flow. Cross-current sedimentation is thoroughly investigated and simulations that use thus obtained results are summarised. The results of the experimental program and of simulations reveal that the capacity of cross-current lamella tanks can be increased tenfold or sedimentation efficiency can be vastly improved. Accordingly, a computer-assisted design of a cross-current tank with the capacity of $100\text{ m}^3/\text{h}$ is made. Such an installation will be most useful in high-efficiency clarification of suspensions from industrial processes or from water purification and waste treatment systems.

Keywords: *cross-current sedimentation, lamella packs, settling tanks, water clarification*

Nomenclature

| | |
|----------------|---|
| ρ, ρ_0 | – density of solid phase and of liquid phase, respectively, |
| μ_0 | – dynamic viscosity, |
| p_w | – specific surface of the lamella packet, |
| F, F_1, F_2 | – settling surface areas, |
| Q | – suspension flow rate, |
| q | – surface loading, overflow rate, |
| d | – equivalent particle size (diameter), |
| d_g | – critical grain size, |
| v, v_g | – settling velocities of particles of the size d, d_g , respectively, |
| $f(d)$ | – probability function of grain diameter, |
| $f(v)$ | – probability function of settling velocity, |
| $\Phi(a)$ | – distribution function in the log-normal distribution $N(0.1)$, |
| $\Phi^{-1}(a)$ | – fractile of the normal distribution $N(0.1)$, |
| m, σ | – parameters of the log-normal distribution of particles size, |
| $\Gamma(a)$ | – Euler's gamma function, |
| $\Gamma(a, b)$ | – incomplete gamma function, |
| d_0, p, n | – parameters in the generalised gamma distribution of the particles size (scale parameter, shape parameters), |
| η | – sedimentation efficiency. |

1. Introduction

Lamella tanks are now in widespread use in water and wastewater treatment installations. They belong to a group of sedimentation tanks whose running costs are relatively low, and investment costs – quite high. That refers particularly to conven-

tional rectangularly shaped or round Dorr clarifiers. When the running costs are on a low level, it is possible to vastly reduce the investment costs.

That is why lamella tanks are receiving a great deal of attention from those sectors of industry which, on account of process requirements or environmental considerations, handle large amounts of suspensions. This group includes the mining and minerals processing sectors and municipal utilities. The chief improvement in lamella sedimentation tanks is an increased flow rate of suspension or enhanced sedimentation efficiency, or the combination of both.

Sedimentation of Blood Corpuscles.

I HAVE noticed lately that if oxalated or defibrinated blood is put to stand in narrow tubes, the corpuscles sediment a good deal faster if the tube is inclined than when it is vertical. Thus with tubes about 2.7 mm. internal diameter there were, after 20 hours, 4, 23, 35, and 42 per cent. of clear serum with tubes inclined at 0°, 22½°, 45°, and 67½° respectively. In another rough experiment with tubes of different diameters, all filled to a height of 40 mm. with diluted blood, after 5 hours there were the following proportions of clear serum :—

| mm. diam. | Vertical Per cent. | 11½° Per cent. | 22½° Per cent. | 33½° Per cent. |
|-----------|-----------------------|-------------------|-------------------|-------------------|
| 2.7 | 6 | 20 | 29 | 51 |
| 8 | 5 | 10 | 15 | 21 |
| 14 | 4 | 5 | 9 | 12 |

The phenomenon seems to depend on the vertical height of the columns of blood, and it occurs to me that the slight Brownian movement of the lower corpuscles may interfere with the sedimentation of those above. But I should be glad if someone would tell me the explanation: the phenomenon is perhaps well known in some other form. A. E. BOYCOTT.

Medical School, University College Hospital, W.C.

Three lamella sedimentation systems available presently are shown schematically in Figure 3: counter-current, co-current and cross-current flow systems.

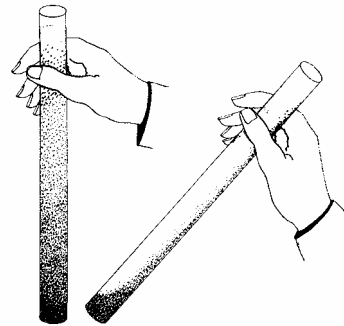


Fig. 1. Press cutting from "Nature" relating to Boycott's effect

Fig. 2. Visualisation of Boycott's experiment [35]

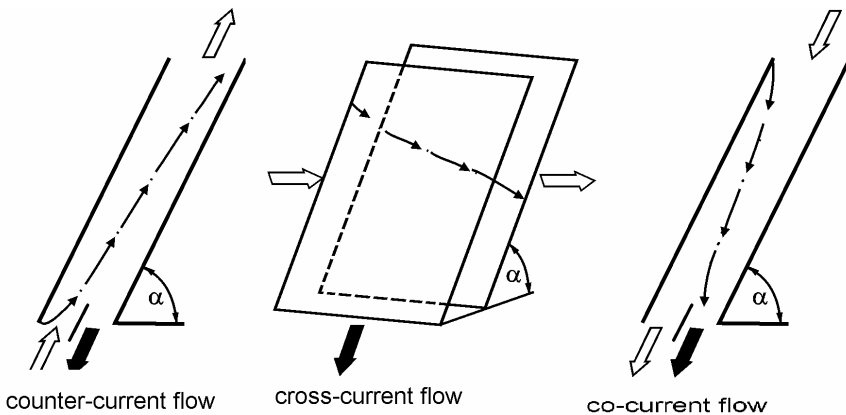


Fig. 3. Lamella process systems

The counter-current system, where the suspension flows in the direction opposite to that of the sliding particles, is now most widely applied. Sedimentation proceeds in conduits made of corrugated plates. A lamella packet of the *envised* type, manufactured in Poland, is shown in Figure 4. The lamella packet performance depends on the relative length of conduits. Engineering the tubes with the relative length over 10 is quite a difficult task.

The cross-current flow system comes next in the ranking list. In the cross-current configuration, the suspension flows horizontally and the sediment flows along the inclined plates in the direction normal to that of the suspension movement. This arrangement seems to be most attractive because, unlike the counter-current systems, an increase in the settling surface is not restricted by design data.

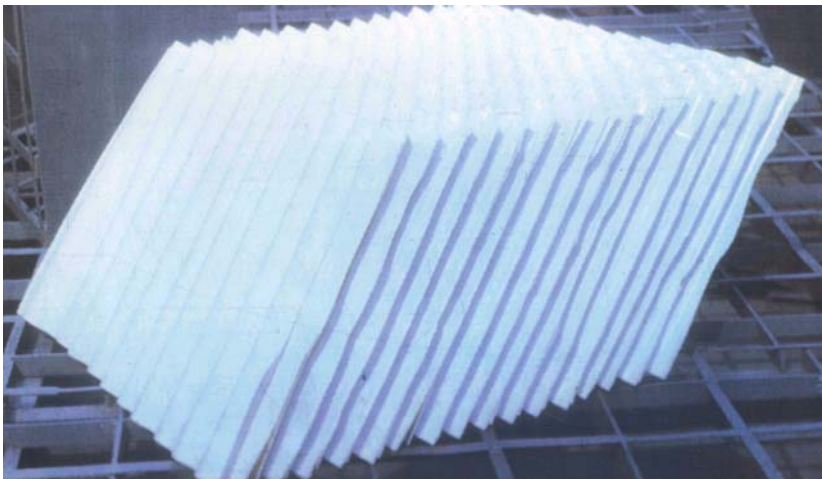


Fig. 4. Lamella packet of the *envised* type

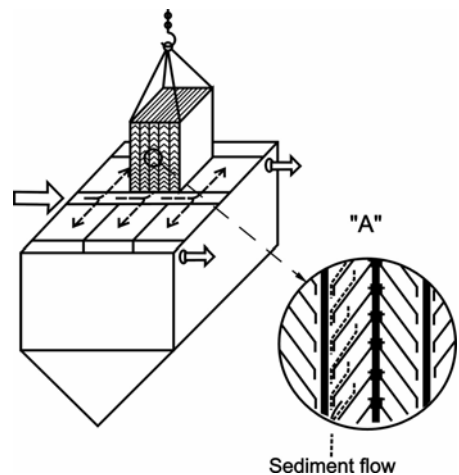


Fig. 5. Diagram of the SERPAC tank

Figures 5 and 6 show counter-current packets used to modernise the existing rectangularly shaped tanks [9].

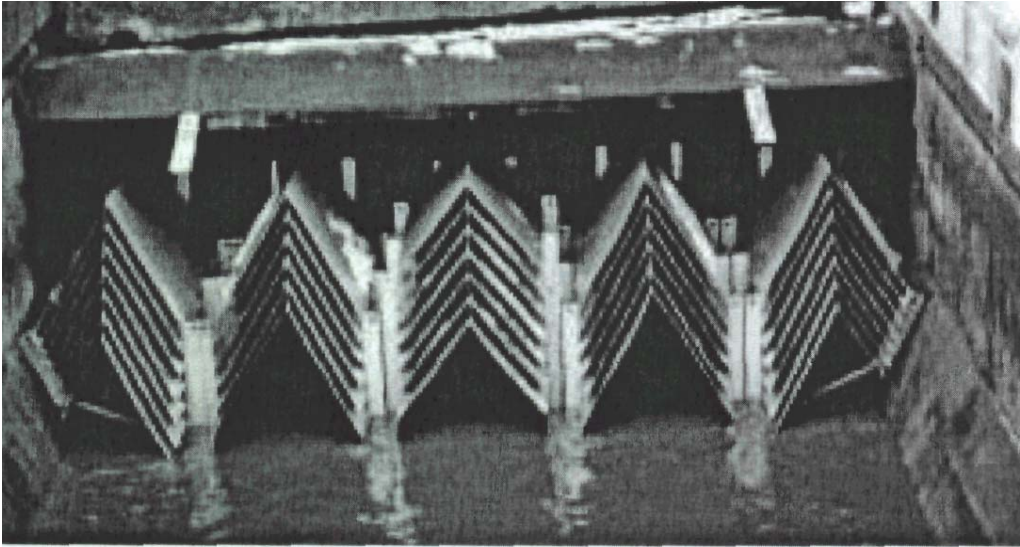


Fig. 6. Application of counter-current lamella packets in an existing tank [9]

The parallel flow system, where the suspension flows downwards in the same direction as the settling particles, seems the least popular and its applications are but a few because the clarified suspension and thickened sediment will mix while leaving the sedimentation area. Nonetheless, a parallel flow system works really well as a sludge thickener.

2. Investigations of cross-current sedimentation processes

Cross-current lamella systems have been extensively studied in several research centres [12, 24], the main objective being to find out how lamella packet surface and configuration should affect sedimentation efficiency and tank performance.

2.1. Experimental set-up

A new original experimental stand at the AGH (University of Science and Technology) allows full-scale investigations of cross-current lamella processes. Results of the experimental programme were used to formulate the guidelines for the design of an industrial tank with the capacity of 100 m³/h. The computer model of the tank is also developed. The experimental set-up has two main elements (see Figure 5):

1. Rectangularly shaped tank with cross-current lamellas, consisting of a feed supply chamber, an overflow collector, an underflow collector or, alternatively, small sediment collectors.
2. Support structure.



Fig. 7. Experimental set-up: sedimentation tank and a supporting structure

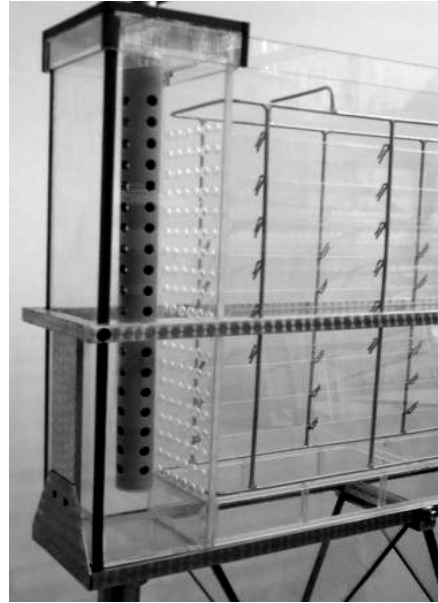


Fig. 8. Feed supply/flooding chamber and a portion of lamella packets

The model of a cross-current sedimentation tank is made of organic glass plates (5 mm thick) and has three major components: a feed supply chamber, a sedimentation chamber and an overflow chamber.

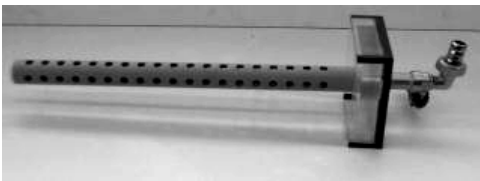


Fig. 9. Tube supplying the feed in a horizontal configuration



Fig. 10. Movable plate ensuring a uniform distribution of the suspension

The feed supply chamber (Figure 7) $100 \times 100 \times 500$ mm is provided with a perforated dosing tube (Figure 9) connected to a dosing valve (ball valve $\frac{3}{4}$ ") mounted in a cover.

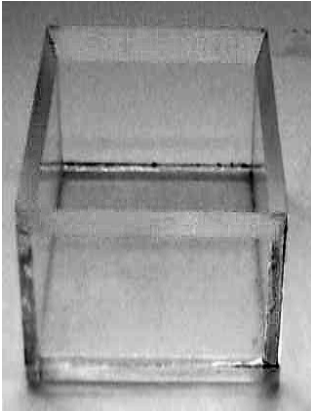


Fig. 11. Sediment collector



Fig.12. Hoppers for sediment collection

The valve is screwed indirectly in the chamber cover. The precise finish of the cover edge ensures that the dosing tube coincides with the chamber axis. The holes in the dosing tube open to the sidewalls and the wall opposite to the sedimentation chamber. At the bottom the tube is secured with a cork which prevents the feed flow into the supply chamber as well as mixing and drifting of sediment collected in the first settling tray (Figure 9). Hence the mass of sediment retained in the supply chamber can be precisely established.

The supply chamber is separated from the sedimentation chamber by a removable corrugated panel (Figure 12).



Fig. 13. Cross-current lamella packets in the sedimentation chamber

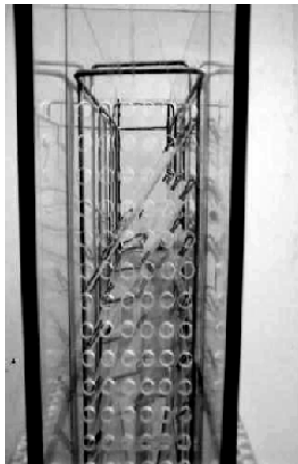


Fig. 14. A plate distributing the suspension – general view



Fig. 15. Overflow-collecting pipe

The corrugations on the dosing tube and the separating panel aimed at stabilising the feed flow in the sedimentation chamber. The sedimentation chamber (Figure 5) is equipped with a settling system and two suspended collecting hoppers with discharge valves (ball valves $\frac{1}{2}$ ") (Figure 10).

On the skeleton structure hatches appear which seem to be an securing the supporting plates inclined at 55° . Six such plates are mounted in that position (Figure 11). Supporting plates are made of organic glass, 1.5 mm thick.

Sediment is collected by two hoppers dividing the tank bottom into two equal parts. Hoppers have bolted ball valves $\frac{1}{2}$ ". The design of the sedimentation chamber allows mounting settling trays over the hoppers, these trays dividing the sedimentation chamber into five equal settling zones. Sediment collected in trays can be subjected to quantitative analysis as well as grain size distribution analysis. When no settling trays are provided, the sedimentation chamber is equipped with an openwork insert which can be fixed in the same position. The insert is made of organic glass rods of rectangular cross-section. The sedimentation chamber is separated from the overflow chamber by a thin panel wall made of organic glass, 5 mm thick.

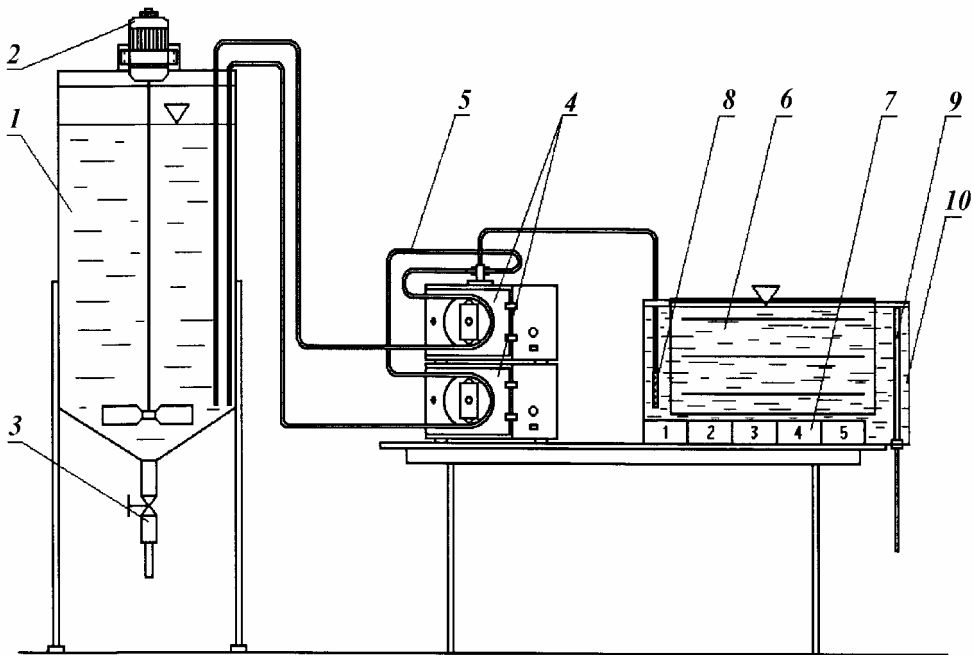


Fig. 16. Experimental set-up: 1—feed tank, 2—mixer drive, 3—outflow from the feed tank, 4—peristaltic pumps, 5—conduits transporting the suspension, 6—cross-current lamella packets, 7—feed inflow to the settling tank model, 9—overflow collector, 10—cross-current flow tank model

The overflow chamber is 100 mm in width, 100 mm in length and 500 mm in height. Half-way up the chamber is a discharge ball valve $\frac{3}{4}$ " (Figure 13). The thread is cut in the organic glass cube, glued to the chamber wall and sealed with a silicone band.

The whole tank is made of transparent materials enabling easy and full monitoring of sedimentation processes. Ball valves ensure smooth regulation and fast control of flow rate. The glue Acrifix 116, intended for organic glass exclusively, provides durable, fast holding and tight proof connection as long as the gluing procedure is pursued in the prescribed manner.

The settling tank is mounted on the supporting structure made from stainless steel. The upper section of the frame is made of rods with rectangular cross-section and the lower part is made of a flat bar and two plates to mount the supply and overflow chambers. The settling chamber is positioned between the two flat bars. Half-way along, on the spot where collecting hoppers are connected, there is a bracket supporting the settling tank and making the load-bearing structure more rigid. Bushings fixing the supports are welded to each of the plates. The lower parts of the supports are mounted in footings made of steel St3Sx coated with an epoxy dye and a surface varnish, as corrosion control measures. The supports are made of stainless pipes.

In accordance with the design objectives, the structural elements are easy to assemble and disassemble. Most elements of the stand are secured with set screws. The openwork construction allows full monitoring of sedimentation processes.

The experimental set-up shown schematically in Figure 16 includes: a feed tank, a mixer arm, peristaltic pumps, conduits transporting the suspension, cross-current lamella packets, collectors of thickened sediment, the model of a cross-current tank.

2.2. Results

The main objective of the tests was to explore how to modernise the clarification system in a battery recycling installation. The two-stage clarification process was designed: in a Dorr clarifier and in a cross-current lamella tank. The sample analyses were collected accordingly.

Representative results are shown in Figure 17.

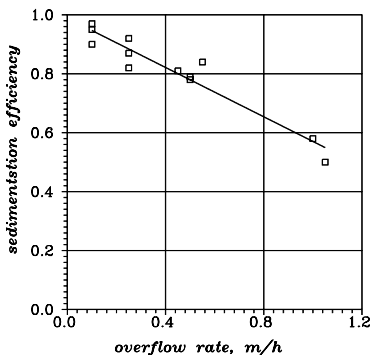


Fig. 17. Sedimentation efficiency versus overflow rate in cross-current sedimentation

The solid phase content in the feed material ranges from 40 kg/m³ to over 120 kg/m³. The solid phase content in the overflow falls between 0.800 kg/m³ and 0.120 kg/m³. These results are consistent with our predictions. The effects of modernisation can therefore be regarded as satisfactory. However, it is anticipated that solid phase content in water treated in a Dorr clarifier might be exceeded in the future and that is why the two-stage clarification is provided. The second-stage clarification proceeds in a cross-current lamella tank.

2.3. Mathematical model of cross-current sedimentation

The starting point is Hazen's theory of sedimentation and its generalisations suggested by Kowalski [20, 21], who has demonstrated that Hazen's sedimentation theory applies just as well to tanks with an inclined bottom [16] and that idealisation of suspension flow in elementary lamella conduits is responsible for slight undervaluing calculation results, at the same time the calculations become easier and less cumbersome. Taking into account the specialists' opinions [1–7, 26, 35], results of tests, calculations and computer simulations, the authors provide below an algorithm based on the works quoted above.

An assumption is made that the whole surface available in a sedimentation tank is a major determinant of the process efficiency. When the tank is not filled with lamella packets, the settling surface is taken as equal to the design value, in other words it equals the surface of the water table. In a tank filled with lamella packets, two settling surfaces are distinguished: that without and that with lamella packets (F_1 and F_2 , respectively). The surface F_2 contained in the packet conduits is obtained as the product of the surface occupied by the packet layer and the specific surface factor p_h . The specific surface factor p_h is determined on the basis of design parameters of the lamella packet and complex features of suspension flow (developing laminar flow, well developed laminar flow or flow with the rectangularly shaped velocity distribution pattern). The specific surface factor p_h indicates how many times the settling surface available in a lamella packet is greater than the surface occupied by the packet. It was shown in [17] that surface areas F_1 and F_2 are additive as long as certain assumptions are made. For convenience the sum $F_1 + F_2$ is used in further calculations as the available settling surface. Knowing the suspension flow rate Q , we obtain the surface load q equal to the settling velocity of critical grains in the given process conditions:

$$q = \frac{Q}{F_1 + F_2} \frac{Q}{F} = v(d_g). \quad (1)$$

The settling velocity $v(d_g)$ of critical grains is derived on the basis of the analysis of particles' flow in liquids (governed by Stokes formula), where ρ and ρ_0 stand for solid phase and liquid phase density, respectively, μ_0 is dynamic viscosity and g is acceleration of gravity:

$$v(d_g) = \frac{1}{18} \frac{(\rho - \rho_0)g}{\mu_0} d_g^2. \quad (2)$$

Formula (2) yields the critical grain size d_g . Knowing the type of statistical distribution of solid phase grain size $f(d)$ and the distribution parameters obtained from grain-size measurements, we obtain the sedimentation efficiency η :

$$\eta = 1 - \int_0^{d_g} f(d) dd + \int_0^{d_g} d^2 f(d) dd. \quad (3)$$

The actual formulation of (3) depends on the type of solid phase particle-size distribution $f(d)$. For some specific cases analytical solutions [22] are provided. When the grain-size distribution $f(d)$ follows the log-normal pattern with the density function of the parameters m and σ (the mean value and standard deviation of the distribution of grain-size natural logarithms)

$$f(d; m, \sigma) = \frac{1}{\sqrt{2\pi}d\sigma} \exp\left(-\frac{1}{2}\left(\frac{\ln d - m}{\sigma}\right)^2\right), \quad (4)$$

then for the argument a the analytical form of (3) related to the distribution function $\Phi_N(a)$ holds:

$$\begin{aligned} \eta(d_g; m, \sigma) = & 1 - \Phi_N\left(\frac{\ln d_g - m}{\sigma}\right) \\ & + \exp\{2 \cdot [\sigma^2 - (\ln d_g - m)]\} \cdot \Phi_N\left(\frac{\ln d_g - m}{\sigma} - 2 \cdot \sigma\right). \end{aligned} \quad (5)$$

When the solid phase particle-size distribution $f(d)$ follows the generalised gamma distribution with the density function of the parameters d_0 , n , p (scale parameter and shape parameters):

$$f(d; d_0, p, n) = \frac{n}{d_0 \Gamma(p)} \left(\frac{d}{d_0}\right)^{pn-1} \cdot \exp\left[-\left(\frac{d}{d_0}\right)^n\right], \quad (6)$$

Equation (3) is rewritten as:

$$\eta(d_g; d_0, p, n) = 1 - \frac{\Gamma\left[p, \left(\frac{d_g}{d_0}\right)^n\right]}{\Gamma(p)} + \left(\frac{d_0}{d_g}\right)^2 \cdot \frac{\Gamma\left[p + \frac{2}{n}, \left(\frac{d_g}{d_0}\right)^n\right]}{\Gamma(p)}. \quad (7)$$

$\Gamma(a)$ is a well-known Euler's gamma function and $\Gamma(a, b)$ is the incomplete Euler's gamma function:

$$\Gamma(a, b) = \frac{1}{\Gamma(a)} \int_0^b x^{a-1} \cdot e^{-x} dx. \quad (8)$$

With reference to (8) we write:

$$a = p \quad \text{or} \quad a = p + \frac{n}{2}, \quad b = \left(\frac{d_g}{d_0}\right)^n. \quad (9)$$

In order to compute the sedimentation efficiency from (5) or (7), we ought to know the parameters of the grain-size distribution and the critical grain size d_g . Parameters of the statistical distribution of the solid phase particle size are obtained from granulometric analysis [18, 19].

Theoretical considerations of computations of sedimentation efficiency of polydisperse suspensions seem rather complicated though the available computer techniques render the task feasible. All the same, the model can be simplified by assuming one of the boundary velocity distributions, so as to have it developed laminarly or rectangularly shaped. The calculation procedure becomes less complicated, though less accurate. According to the authors, this inaccuracy is fully acceptable in the investigations of dilute suspensions.

2.4. Computer simulations

Computer simulations of cross-current sedimentation processes are based on the mathematical model presented above. Simulation procedures involved the calculation of sedimentation efficiency for the assumed tank geometry, physical properties of the suspension and its flow rate.

Geometric parameters of the tank are expressed in terms of the settling area dependent on the tank dimensions, the number of plates making up the lamella packet and plate inclination angle. The following parameters of the suspension were considered: solid and liquid phase density, temperature of the suspension expressed in terms of the dynamic viscosity and solid phase grain-size distribution, represented by the distribution pattern of a random variable. For the purpose of simulations, the grain-

size distribution is assumed to be log-normal.

Suspension flow rate and settling surface (i.e. tank geometry parameters) are expressed as the surface load factor – the flow rate to settling surface ratio. Having obtained the surface loading, solid phase and liquid phase density and dynamic viscosity of the liquid phase, the particle sizes were determined for the given process conditions.

Therefore, computer simulations are brought down to the calculation of sedimentation efficiency as the function dependent on surface loading q and enveloping tank geometry, suspension flow rate, physical properties of the suspension (particularly the solid phase density and grain-size distribution given in terms of log-normal parameters: m – mean value of natural logarithms of particle size and σ – standard deviation of particle sizes' natural logarithms).

Formally, the relationship applied in simulations:

$$\eta = f(q, m, \sigma, d_g), \quad (10)$$

where

$$q = \frac{Q}{F} = v(d_g), \quad (11)$$

$$d_g = \sqrt{\frac{18 \cdot \mu_0}{(\rho - \rho_0) \cdot g} \cdot q}. \quad (12)$$

The dynamic viscosity is determined from the formula:

$$\mu_0 = \frac{1.79 \cdot 10^{-3}}{1 + 0.0337 + 0.000222 \cdot t^2}, \quad (13)$$

where t stands for suspension temperature [°C]. The suspension temperature is assumed $t = 20$ °C and the dynamic viscosity μ_0 is equal to $1 \cdot 10^{-3}$ kg/m/s.

Selected results of computer simulations are shown in Figures 19–26. Sedimentation efficiency is plotted as the function of surface loading (in the range of 0–1.5 m³/m²/h) for the specified values of log-normal parameters: $m = 2.0, 2.5, 3.0, 3.5$ and $\sigma = 0.6, 1.0$. In each case, five curves are plotted to show the influence of the solid phase particles density $\rho = 2000, 3000, 4000, 5000, 6000$ kg/m³.

It is readily apparent that the influence of the surface loading is essential. In the case of suspensions containing the finest solid particles ($m = 2, \sigma = 0.6$, see Figure 17) the sedimentation efficiency over 0.8–0.9 is achievable, provided that surface loading

cannot exceed the value of $0.15 \text{ m}^3/\text{m}^2/\text{h}$, no matter what the solid phase density. The influence of the solid phase density is vital when the sedimentation efficiencies achieved turn out to be low. For example, for a surface loading of $1 \text{ m}^3/\text{m}^2/\text{h}$ the sedimentation efficiency of particles with the density of $6000 \text{ kg}/\text{m}^3$ is 0.6, while for the particles' density of $2000 \text{ kg}/\text{m}^3$ it will be slightly more than 0.2.

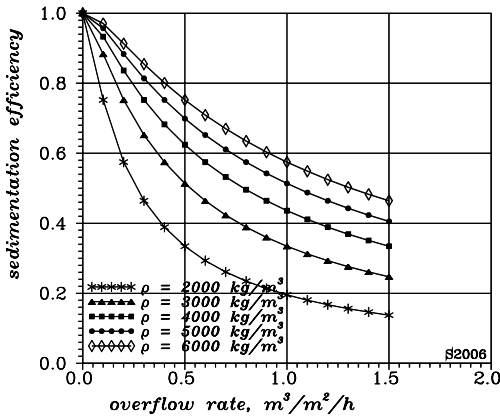


Fig. 18. Sedimentation efficiency versus surface loading for $m = 2.0$ and $\sigma = 0.6$

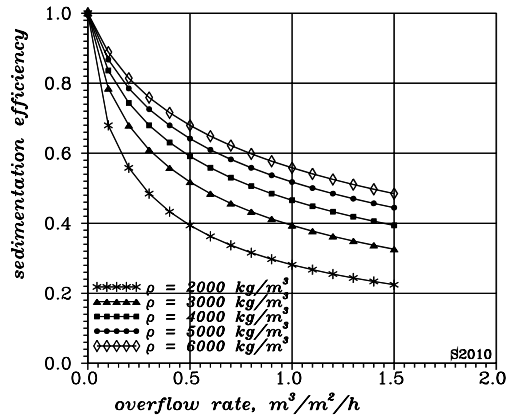


Fig. 19. Sedimentation efficiency versus surface loading for $m = 2.0$ and $\sigma = 1.0$

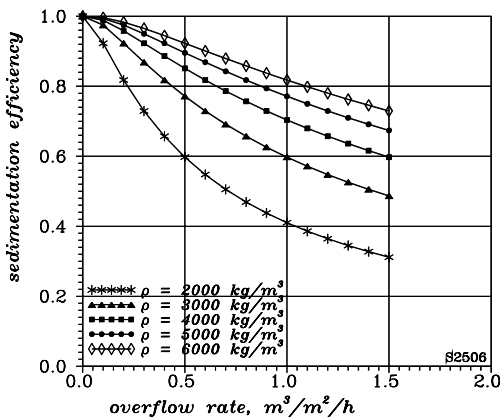


Fig. 20. Sedimentation efficiency versus surface loading for $m = 2.5$ and $\sigma = 0.6$

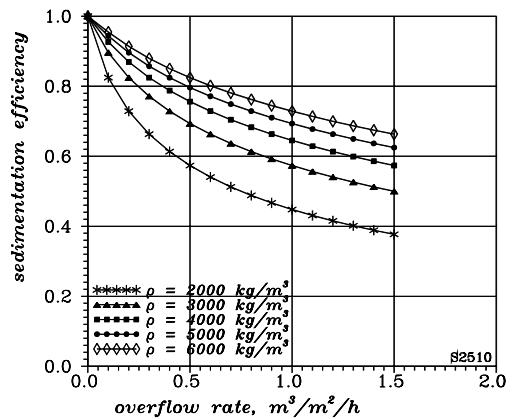


Fig. 21. Sedimentation efficiency versus surface loading for $m = 2.5$ and $\sigma = 1.0$

Results of computer simulations might be used in preliminary evaluation of sedimentation efficiency.

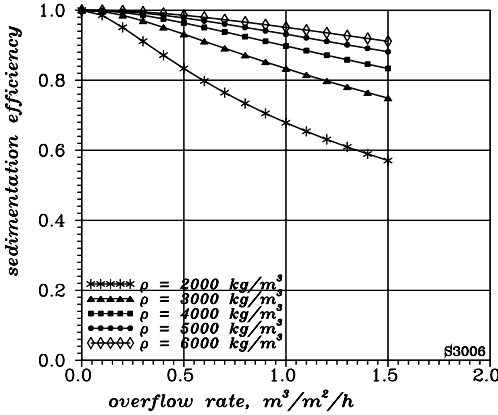


Fig. 22. Sedimentation efficiency versus surface loading for $m = 3.0$ and $\sigma = 0.6$

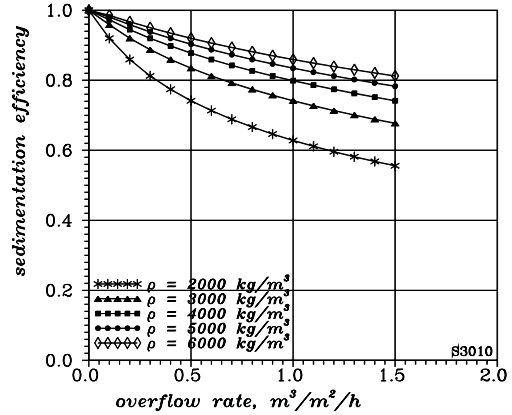


Fig. 23. Sedimentation efficiency versus surface loading for $m = 3.0$ and $\sigma = 1.0$

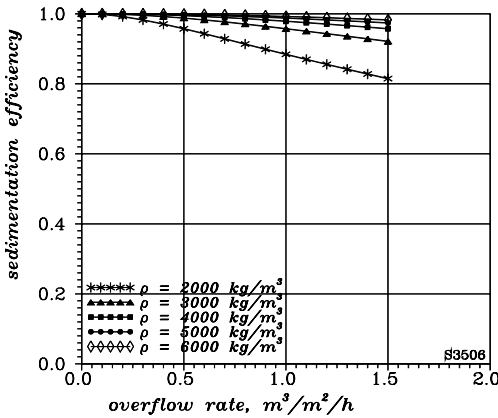


Fig. 24. Sedimentation efficiency versus surface loading for $m = 3.5$ and $\sigma = 0.6$

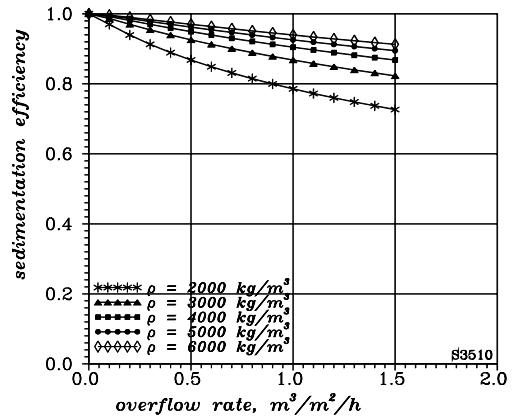


Fig. 25. Sedimentation efficiency versus surface loading for $m = 3.5$ and $\sigma = 1.0$

3. Design of a cross-current sedimentation tank

These design guidelines have their relevance to the new prototype of a cross-current lamella sedimentation tank intended for clarification of suspensions from the first-

stage treatment process in a Dorr clarifier. The input data for the design are the results of investigations and simulations summarised in the previous chapters.

Suspension flowing at the rate of approximately $120 \text{ m}^3/\text{h}$ enters the cross-current tank, about $20 \text{ m}^3/\text{h}$ of the suspension will be discharged via an underflow. Thus we obtain the flow rate of about $100 \text{ m}^3/\text{h}$ of the suspension with the solid phase content nearing zero.

Extensive tests and simulations reveal that surface loading in the tank should not exceed $0.25 \text{ m}^3/\text{m}^2/\text{h}$ and hence the settling surface should be at least 400 m^2 . It is suggested that two “twin” tanks be built. Application of 25 lamella packet segments is feasible, thereby increasing the settling surface 25-fold in relation to the surface occupied by the packets. Let the base of the working unit of one tank have the surface area of 10 m^2 . The available settling surface will be 250 m^2 , leaving a safety margin of 20%.

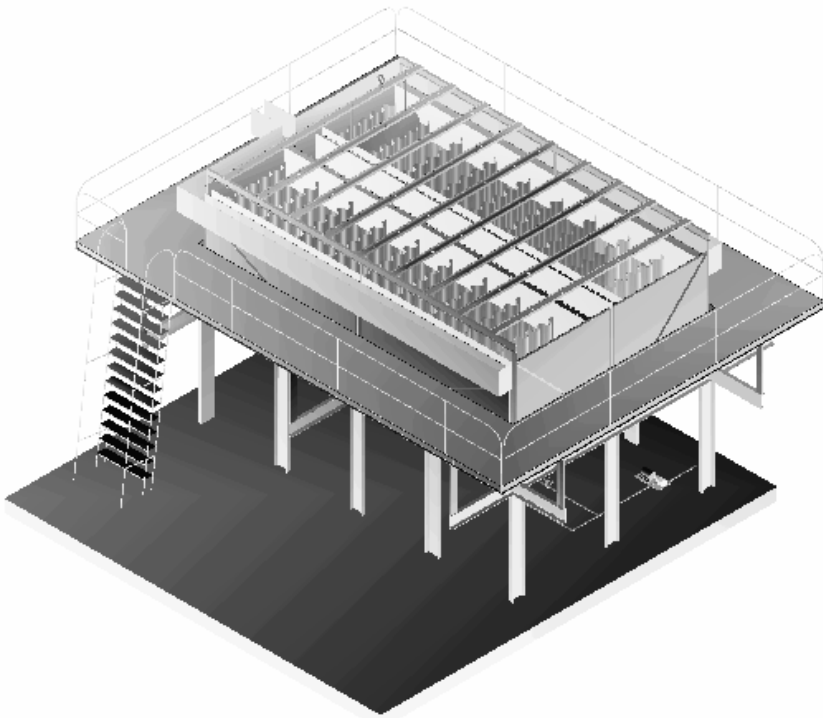


Fig. 26. Model of cross-current sedimentation tank – general view

In the preliminary stage of design, it is assumed that the tank housing will be made of steel, though other options are considered, too. The housing might be also made of plastic materials and that solution offers several benefits: resistance to corrosion and

vastly reduced maintenance costs. However, the cost of constructing a plastic frame will be decidedly higher.

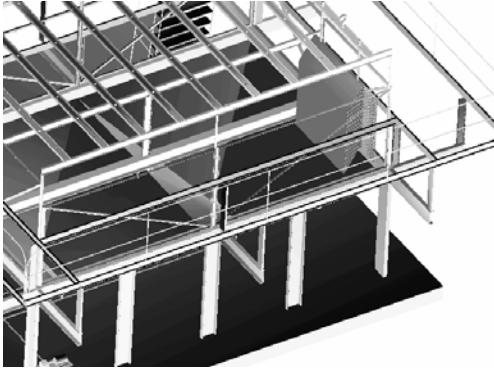


Fig. 27. Tank structure without wall, with a single lamella packet

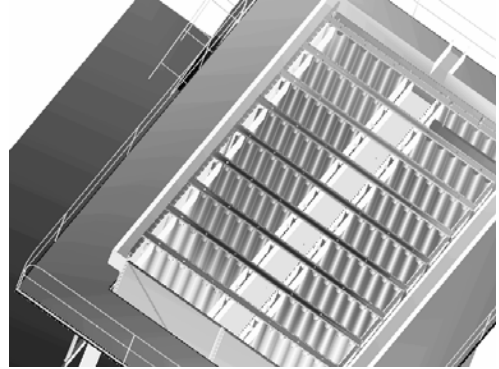


Fig. 28. Model tank interior

The computer model of a cross-current sedimentation tank and the selected details are shown in Figures 27–31. The computer model is shown as a single still from a computer-processed film showing the spatial view and tank interior as well as subsequent steps of the tank assembly.

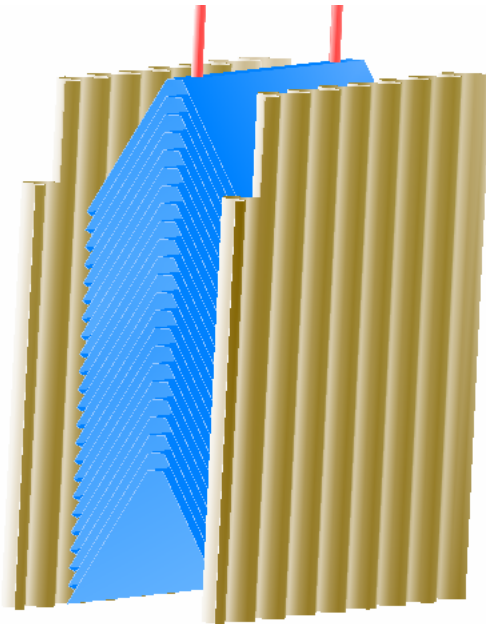


Fig. 29. Lamella packet (herringbone pattern)

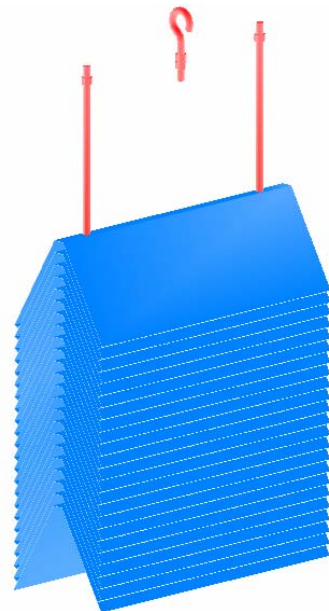


Fig. 30. Lamella packet (herringbone)

and the chamber wall

pattern) and the lifting sling

Main design guidelines:

1. The key element securing the housing in place is the frame made of the standard C-profiles. The inside diameter of the frame should be 5050 mm in the direction of the main symmetry axis and 3200 mm in the direction of the short axis.

2. Above the frame arranged horizontally, on the edges parallel to the main symmetry axis there are symmetric shelves running inwards to the distance 100 mm (towards the frame axis) to support the lamella packets. Besides, a similar shelf though twice as wide (about 200 mm) should be placed along the longer axis of the frame.

3. Underneath the frame two hollow chambers intended for sediment collection are provided. They are shaped like pyramids, their vertices directed downwards, the side wall inclination 45° .

4. On the vertices of these two pyramids (at the lowest points in the settling chamber) there are valves connected with pipes used for removing the sediment. Sediment discharge and its further transport to the basin supplying the feed material to the Dorr clarifier should be induced by a pump with the capacity of $20 \text{ m}^3/\text{h}$, operated jointly for the two twin tanks.

5. Around the whole tank on the level of the frame there is a platform about 1 m wide for the personnel.

6. A vertical, split clarification chamber shaped like a rectangular prism minus a bottom and roof is on the frame. Its height approaches 1600 mm.

7. The clarification chamber is divided by a vertical baffle coinciding with the main axis of the frame symmetry and supported on a shelf. The baffle should be about 400 mm lower than the longer chamber walls.

8. Clarified suspension flows out along the outside edges parallel to the longer axis of the chamber, that is why shorter wall ought to be higher than the longer ones.

9. The feed supply basin is over the baffle. It should be 400 mm wide and 500 mm high, out of which 100 mm should extend above the liquid level and 400 mm is kept immersed. The bottom of the chamber (in its axis of symmetry) is tangent to the upper edge of the baffle. The connection between the baffle and the basin bottom need not be sealed.

10. The flow of suspension from the Dorr clarifier overflow to the supply basin is induced by the forces of gravity. It is suggested that the suspension flowing in the pipeline over the chamber be distributed in three pipes symmetrical in the plane of the baffle.

11. In the basin bottom, there is a plugged drain, easy to open (similar to the one in a bath tub). It is used to empty the feed basin whilst the whole tank is being emptied.

12. Suspension flows from the feed supply basin into two symmetrical sections of the chamber. It flows in the horizontal direction, parallel to the shorter axis of the

chamber. The flow path equals 1600 mm (half-width of the chamber). From the chamber filled with lamella packets the suspension flows to the overflow basin.

13. Overflow basins are fixed along the longer walls of the split chamber. On one of the shorter walls there is the trough connecting the overflow basins so that the whole clarified suspension leaves the system.

14. Each of the twin chambers is divided into 10 sections by vertical panels made from corrugated plastic plates, with the wave height of 50 mm. Dividing panels are supported on shelves on the frame level and extend over the liquid table (over 100 mm). Single section dimensions are: 1600 mm (split chamber width) \times 500 mm (section width taking into account the width of a corrugated panel).

15. Each section (including the first and the last one) is surrounded by two parallel corrugated baffles. One baffle is used between each two neighbouring sections (apart from the first and the last one).

16. At the bottom of each section an extra bottom surface is provided: a protective barrier directing the suspension towards the section interior. The barrier is made of PVC board shaped like a sloped roof inclined at 60° with a horizontal ridge 40 mm in width. The barrier length equals the width of the split chamber (identical to the section length equal to 1600 mm). The barrier is supported on shelves lying on the frame.

17. Each section has two saw-tooth edges, their height variable and controllable over 50 mm to ensure the equal chamber loading.

18. On the end of feed basin each section is provided with a guiding barrier, directing the suspension downwards. The guiding barrier is located at the distance of 100 mm from the feed supply basin and extends over the liquid level (about 100 mm), the remaining part (i.e. 500 mm) should be immersed.

19. On the overflow basin end each section has a guiding barrier different from the previous one in that that it should be immersed to the depth of about 200 mm.

20. In each section, there are lamella packets. Packets are arranged in a herring-bone pattern, the elementary unit being a symmetrically shaped profile resembling a roof inclined on both sides and with a flat ridge. The inclination angle of the profile is 60° . The terminal edges are bent at the right angle so that each profile be supported on the previous one. In the bend sections, some openings are cut, accounting for 80–90% of the bend surface. The single packet contains 25 shaped profiles. Shaped profiles are interconnected by two vertical tubes 1500 mm in length and with the outside diameter 10 mm. These tubes pass through the openings made in the ridges of the shaped profiles. Between the subsequent profiles there are spacing elements (bushings) with washers. The height of the spacing elements is 40 mm. In the lowermost tube section, there is a back nut with a washer. In the topmost tube section, a hook is provided to hang the packet. Hooks are hung on a rod coinciding with the section axis, at the height of 200 mm over the liquid level. A screw joint between the hook and the tube enables position control of the packet inside the section (in a range of about 50 mm). The rod is supported on a framework connected to the split chamber. Inside the section the packet is tangent to the ridges of corrugated baffles.

4. Conclusions

Theoretical studies and computer simulations of cross-current processes in sedimentation tanks with lamella packets reveal that tank capacity during clarification of dilute suspensions can be vastly improved if compared with the conventional tanks (even ten-fold increase of process capacity is reported). As regards the lamella counter-current processes, the improvement in performance is two- or even three-fold, in relation to the space they occupy.

It appears, therefore, that cross-current sedimentation tanks can successfully be applied in industrial installations for clarification of suspensions which, on account of the presence of very fine particles or the flow rates, are hard to process because of space limitations and high costs. In many sectors of industry, suspensions are clarified in installations designed many years ago and the achievable sedimentation efficiencies are regarded as insufficient in the light of the present standards. In such cases, the use of cross-current lamella tanks as secondary clarifiers might be the answer to the problem, ensuring the required quality of clarified suspension at relatively low costs, estimated to be 20% of costs involved in construction of traditional tanks.

High capacity of cross-current lamella tanks (or improved sedimentation efficiency) are achievable by extending the settling surface thanks to the placing of lamella packet sections at small intervals. The presence of lamella packets causes no problems during the clarification of dilute suspensions though when thickened suspensions are handled, the clarification processes might be disturbed.

References

- [1] Bandrowski J., Hehlmann J., Merta H., Ziolo J.: *Opracowanie metody optymalnego doboru wysokosprawnych osadników z wypełnieniem na podstawie doświadczalnych badań osadników*, Inż. Ap. Chem., 1 (1997), 3–8.
- [2] Bandrowski J., Hehlmann J., Merta H., Ziolo J.: *Podział zawiesin ze względu na możliwość zagęszczania w osadnikach z wypełnieniem oraz analiza czynników wpływających na proces sedymentacji cienkowarstwowej*, Inż. Ap. Chem., 3 (1997), 3–7.
- [3] Bandrowski J., Hehlmann J., Merta H., Ziolo J.: *Studies of sedimentation settlers with packing*, Chem. Engng. and Proc., 36, (1997), 219–229.
- [4] Bandrowski J., Merta H., Ziolo J.: *Analiza modeli osadników z wypełnieniem*, Inż. Ap. Chem., 6, 1995.
- [5] Bandrowski J., Merta H., Ziolo J.: *Sedymentacja zawiesin. Zasady i projektowanie*, Wyd. Politechniki Śląskiej, Gliwice, 2001.
- [6] Bandrowski J., Merta H., Ziolo J.: *Analiza modeli osadników z wypełnieniem* (in Polish), Inż. Ap. Chem., 6, 1995.
- [7] Bandrowski J., Merta H., Ziolo J.: *Modele osadników z wypełnieniem*, Mat. XVI Ogólnopolskiej Konferencji Naukowej Inżynierii Chemicznej i Procesowej, t. 1. *Przepływy, mieszanie. Procesy dynamiczne z fazą stałą*, s. 180–185, Wyd. Politechniki Gdańskiej, 12–15 września 1995.

- [8] Buer T., Margraf M.: *Enhancement of activated sludge plants by lamellas in aeration tanks and secondary clarifiers*, Paper presented at the Aeration Conference on Applied Techniques to Optimize Nutrient Removal and Aeration Efficiency, Helsinki, 2000.
- [9] Boycott A.E.: *Sedimentation of Blood Corpuscles*, Nature, 104, 532.
- [10] Camp T.R.: *Sedimentation and the Design of Settling Tanks*, Trans. Amer. Soc. Civ. Engrs, 111, 1946, 895–958.
- [11] Gęga J.: *Wysokosprawne osadniki z wkładami rurowymi do oczyszczania ścieków hutniczych*, Zesz. Nauk. AGH, 561, 9, 1976, 89–99.
- [12] Haba J., Nosowicz J., Pasiński A.: *Klären und Eindicken von Suspensionen in Lamelleneindickern*, Aufbereitungs-Technik, 4, 1980, 198–201.
- [13] Haba J., Nosowicz J., Pasiński A.: *Sedymentacja zawiesin w osadnikach płytowych*, Rudy Metali, 23, 9, 1978, 440–444.
- [14] Haba J., Nosowicz J., Pasiński A.: *Wyznaczanie stopnia sedymentacji w osadniku z wypełnieniem płytowym*, Rap. Inst. Inż. Chem. Urz. Ciepl. Polit. Wrocław, seria preprints, 91, Wrocław, 1980.
- [15] Haba J., Pasiński A.: *Badanie osadnika płytowego w zastosowaniu do technologii otrzymywania wodorotlenku glinu*, Rap. Inst. Inż. Chem. Urz. Ciepl. Polit. Wrocław, 4, Wrocław, 1979.
- [16] Hazen A.: *On Sedimentation*, Trans. ASCE, 53, 1904, 45–88.
- [17] Kowalski W.: *Mathematical model of sedimentation process in the bended suspension stream* (in Polish), Arch. Ochr. Środ., 1–2, 109–120, 1991.
- [18] Kowalski W.: *Parameters of the particles composition of the emitted dust from iron metallurgy processes* (in Polish), Arch. Ochr. Środ., 1–2, 67–79, 1991.
- [19] Kowalski W.: *Sedimentation balance – interpretation method of information about particle composition* (in Polish), Arch. Ochr. Środ., 1–2, 1991, 159–167.
- [20] Kowalski W.: *Generalization of Hazen's Sedimentation Theory*, Archives of Hydroengineering, Vol. XXXIX, 2, 1992, 85–103.
- [21] Kowalski W.P.: *Analiza teoretyczna i badania procesu sedymentacji wielostrumieniowej* (in Polish), Problemy Inżynierii Mechanicznej i Robotyki, 3, Kraków, 2000, 179.
- [22] Kowalski W.P.: *Podstawy teoretyczne projektowania osadników z wkładami wielostrumieniowymi* (in Polish), Zeszyty Naukowe AGH, seria Mechanika, 27, Kraków, 1992, 132.
- [23] Kowalski W. P.: *Modelowanie matematyczne procesu sedymentacji ziaren zawiesin polidyspersyjnych*, Mat. XLIII Sympozjonu pt. „Modelowanie w mechanice” (in Polish), Gliwice, 2004.
- [24] Kujawska E.: *Badania procesu sedymentacji w osadniku z wypełnieniem płytowym i profilowym*, PhD Thesis, Politechnika Śląska, 2003.
- [25] Niedźwiedzki Z.: *Badania teoretyczne i eksperymentalne wypełnień osadników wielostrumieniowych*, Zesz. Nauk. Politechniki Łódzkiej, 863, Łódź, 2000, 162.
- [26] Merta H.: *Projektowanie osadników z wypełnieniem. Część 1. Parametry projektowe i technologiczne osadników płytowych i rurowych oraz ich klasyfikacja* (in Polish), Inż. Ap. Chem., 2, 1996, 3–10.
- [27] Nipl R.: *O zastosowaniu uogólnionego rozkładu gamma do aproksymacji krzywych składu ziarnowego*, Mat. XIII Krakowskiej Konferencji Nauk.-Techn. Przeróbki Kopalnin (in Polish), Kraków, 1979, 323–330.

- [28] Olszewski W.: *Osadniki wielostrumieniowe*, [in:] *Nowa Technika w Inżynierii Sanitarnej* (in Polish), Wodociągi i Kanalizacja, t. 5, 1975.
- [29] Oden S.: *Eine neue Methode zur Bestimmung der Kornverteilung in Suspensionen*, Kolloid -Z , 18, 2, 1916, 33–47.
- [30] Orzechowski Z.: *Przepływy dwufazowe, jednowymiarowe, ustalone, adiabatyczne*, PWN, Warszawa, 1990.
- [31] Papoulis A.: *Prawdopodobieństwo, zmienne losowe i procesy stochastyczne*, wyd. 1, WNT, Warszawa, 1972.
- [32] Mięso R.: *Badania prostopadłoprądowego procesu sedymentacji*, PhD Thesis, AGH, Kraków, 2000.
- [33] Stacy E.W.: *A Generalization of the Gamma Distribution*, *Annals of the Mathem. Statistics*, Vol. 33, 3, 1962.
- [34] Stokes G.G.: *On the Effect of the Internal Friction of Fluids on the Motion of Pendulums*, *Camb. Trans.*, Vol. 9.
- [35] Materiały informacyjne firmy Sala Inc.
- [36] Ziolo J.: *Influence of the system geometry on the sedimentation effectiveness of lamella settlers*, *Chem. Engng. Sci.*, Vol. 51, 1, 1996, 149–153.

Prostopadłoprądowe osadniki wielostrumieniowe

Przedstawiono genezę urządzeń sedymentacyjnych opartych na wykorzystaniu efektu Boycotta. Opisano trzy podstawowe układy, w jakich prowadzi się sedymentację wielostrumieniową. Są to: układ przeciwprądowy, prostopadłoprądowy i współprądowy. Poprawę efektywności sedymentacji w osadnikach z wkładami wielostrumieniowymi osiąga się, zwiększając powierzchnię sedymentacyjną.

Miara zwiększenia powierzchni sedymentacyjnej jest wskaźnik wyrażony przez stosunek pola powierzchni sedymentacyjnej zawartej w pakiecie do podstawy pakietu, nazywany powierzchnią właściwą. Przedstawiono typową konstrukcję pakietu wielostrumieniowego dla sedymentacji przeciwprądowej. Ograniczenia konstrukcyjne (zwiększanie długości przewodu z jednoczesnym zmniejszaniem jego przekroju poprzecznego) i wykonawcze powodują, że nie da się osiągnąć wskaźnika powierzchni właściwej o wartości wyższej od 5–6, a ponadto przepływ zawiesiny w przewodach o długości względnej $l/d > 10$ osiąga zakres dużych liczb Reynoldsa i przestaje być laminarny. Można jednak zastosować inną koncepcję rozwiązania konstrukcyjnego pakietów opartą na wielostrumieniowej sedymentacji prostopadłoprądowej. W tym przypadku ograniczenia konstrukcyjne i wykonawcze nie stanowią przeszkody, pakiet jest, bowiem stosem płyt o teoretycznie nieograniczonej wysokości.

W artykule opisano oryginalne stanowisko do badań sedymentacji prostopadłoprądowej. Przedstawiono także matematyczny model procesu sedymentacji prostopadłoprądowej, wyniki badań oraz wyniki symulacji komputerowych. Wyniki badań i symulacji komputerowych prowadzą do wniosku, że w osadnikach tego typu można nawet ponad 10-krotnie zwiększyć wydajność lub adekwatnie podnieść efektywność sedymentacji. Na podstawie badań i obliczeń przedstawiono komputerowy projekt osadnika prostopadłoprądowego o wydajności $100 \text{ m}^3/\text{h}$. Urządzenie tego typu zajmuje około 10% miejsca niezbędnego dla tradycyjnych urządzeń sedymentacyjnych i pozwala osiągnąć dużą efektywność porównywalną z efektywnością tradycyjnych urządzeń. Dłatego może być stosowane do wysokosprawnego i wysokowydajnego kla-

rowania zawiesin przemysłowych lub zawiesin pochodzących z obiegu uzdatniania wód i oczyszczania ścieków, zwłaszcza w przypadkach, gdy jest brak miejsca na urządzenia tradycyjne lub gdy dąży się do obniżenia kosztów budowy i eksploatacji osadnika.

The analysis of brushing tool characteristics

S. SPADŁO

Kielce University of Technology, al. Tysiąclecia P. P. 7, 25-314 Kielce

In this paper, an analytical procedure is developed in order to evaluate the filament loading of a circular brush. Filament deformation is computed based on the mechanic analysis in conjunction with kinematic constraints for a rigid flat surface with friction taken into account. Numerical results which reveal the relationship between rotation angle and force distribution are reported.

Keywords: *flexible electrode, filament, interaction forces*

1. Introduction

So far the machining process using filamentary metal brushes in the shape of disks has been used in surface machining to remove corroded layers, to prepare metal surfaces to be galvanized, and to produce surfaces of high adhesion to be coated with paint, glue, etc. Recently the process has been developed to include operations such as removing sharp edges and burrs [1,10], flashes and bosses from machine parts made of alloys of non-ferrous metals, as well as cleaning welds. Using brushes with densely packed filaments made of hard steel broadens the range of uses to include the micro-milling of ordinary constructional steels of low hardness, which are machined with the tips of the filaments. To summarize, the typical uses of metal brush tools are limited to machining materials whose hardness is lower than that of the material the filaments of the brush are made of.

Using the filaments made of abrasive-grain-filled polymers allows the brushes to be used to machine the surfaces of materials of high hardness.

On analysis of the advantages of using brush tools the author suggests a new machining operation that combines mechanical, electrochemical, and electro-erosive processes acting on the machined item [3–6].

Due to the synergistic effect this type of hybrid machining makes the metal removal process more cost-effective.

Soft-machining parameters allow not only the removal of the excess material from large items of low stiffness but also the highly efficient volumetric machining of metals, alloys, and conductor-based composites.

The numerous uses of brush electrodes result from such their characteristics as:

- flexibility of individual filaments,
- type, shape, and packing density of the filaments,
- possibility of operating at various settings of electrode deflection,

- large contact zone of the tool and the machined item,
- possibility of using the electrode until it is worn out,
- large working area of the hot electrode allowing the machining of both flat and complex-shape items.

Because of their construction brush electrodes are characterized by:

- uniform distribution of the filaments, which helps to form a discrete structure suitable for maintaining stable conditions in the machining zone,
- radial, axial, and tangential flexibility, which makes the filaments fit easily complex geometry surfaces, thus permitting a uniform removal of surface layers without changing significantly the geometry of the machined part,
- easy disposal of the erosion by products from the discharge zone,
- suitability for automated operations.

The use of brushing tools in an automation environment will necessitate a clear understanding of an important characteristics of brush performance such as forces. An understanding of such characteristics is important, as surface preparation processes require a detailed knowledge of interrelationships between productivity of machining and brush operating conditions [3, 7]. For example, it is recognized that electrical discharges generated during electroerosion-mechanical processes are closely related to the mechanical characteristics of the filament [5].

2. Statics and kinematics of a single filament

Since the elements of a disk brush tend to deform easily, the use of the brush in erosion mechanical machining changes the character of mechanical interactions with the machined surface in contrast to deformation-resistant electrodes. An increase in the value of the pressure force at the filament tip as a function of displacement along the surface inevitably leads to a break in the anodic film and initiates discharges whose frequency can be determined, among others, by the vibrations of individual filaments of the electrode.

The mechanics of the movement and the interactions between the filament wire and the machined surface are very complex. The wire becomes deformed in a way that is difficult to analyse. This is caused by confounded boundary conditions which allow only an approximate solution to the equation of its motion.

Only a tentative analysis of the interactions between the brush elements and the surface has been presented.

Let us consider a tentative analysis of a filament load. The basic assumptions are:

- inertial forces are neglected,
- the filament tip moves along a rigid surface.

Additionally, due to low packing density, interactions between individual wires are ignored. It is assumed that the filaments are placed radially from the hub centre and are restrained at the hub outside radius and obey Hooke's law [8].

$$b = \frac{a+r}{\sin \alpha} - r + h \cos \alpha = d + h \cos \alpha ,$$

$$d = \frac{a+r}{\sin \alpha} - r.$$

We assume that:

$$F_y = \mu F_x,$$

$$F_\xi = c_1 F_x,$$

$$F_\eta = c_2 F_x,$$

$$c_1 = \sin \alpha - \mu \cos \alpha ,$$

$$c_2 = \cos \alpha + \mu \sin \alpha,$$

where:

$$\alpha = \omega_0 t ,$$

μ – coefficient of friction between the filament tip and the machined surface,
 ω_0 – angular velocity of the brush.

The function $\eta(\xi)$ should also satisfy the following condition:

$$l - \int_0^b \sqrt{1 + [\eta'(\xi)]^2} d\xi = 0. \quad (2)$$

It is very difficult to obtain numerical solutions for Equation (1) with constraint (2). Analytical solutions can be obtained if the values of $\eta(\xi)$ are small enough to enable the linearization of the left-hand side of Equation (1).

The details of the solution of Equation (1) with initial conditions:

$$|\eta(0)| = 0 \quad \text{and} \quad |\eta'(0)| = 0$$

and with the assumption that the wire tip (for $\xi = b$) has point contact with the surface (then $\eta''(b) = 0$) have been presented below.

We will examine a case of a single filament load under tentative conditions presented above. The deflection of the part is described in a mobile reference system $K \xi \eta$ (Figure 1). In such a case, $\eta = \eta(\xi)$ is its elastic deflection with the assumption that there is no influence of non-dilatational strain.

An approximate analytical solution can be obtained if we assume that the values of $\eta'(\xi)$ are small enough to enable the linearization of the left-hand side of Equation (1), which is the case where:

$$\frac{l-a}{l} \ll 1.$$

Then we assume that:

$$|\eta'(\xi)| \ll 1.$$

Consequently, in place of Equations (1), (2) we can have

$$EI \left[1 - \frac{3}{2} \eta'^2(\xi) \right] \eta''(\xi) = [C_2(b - \xi) + C_1(f - \eta)] F_x, \quad (1a)$$

$$l - b - \frac{1}{2} \int_0^b [\eta'(\xi)]^2 d\xi = 0, \quad (2a)$$

where:

$$f = \eta(b).$$

As a result of a subsequent approximation the above equations are replaced by:

$$EI \eta'' = [c_2(b - \xi) + c_1(f - \eta)] F_x \quad (3a)$$

$$\frac{1}{2} \int_0^b [\eta'(\xi)]^2 d\xi = l - b. \quad (3b)$$

Furthermore, we will consider solutions for Equations (3) valid only if $l-a$ is small. The first equation is as follows:

$$\eta'' = [c_2 d + (c_2 \tan \alpha + c_1) f - c_2 \xi - c_{1\eta}] \frac{F_x}{EI}$$

and we assign:

$$\omega^2 = \frac{c_1 F_x}{EI},$$

$$\frac{F_x}{EI} = \frac{\omega^2}{c_1},$$

thus

$$\eta'' + \omega^2 = [c_2 d + (c_2 \tan \alpha + c_1) f - c_2 \xi - c_1 \eta] \frac{\omega^2}{c_1} - \frac{c_2}{c_1} \omega^2 \xi,$$

because

$$c_2 \tan \alpha + c_1 = 1 / \sin \alpha,$$

so

$$\eta'' + \omega^2 \eta = D - \frac{c_2}{c_1} \omega^2 \xi, \quad (4)$$

where:

$$D = (c_2 d + h) \frac{\omega^2}{c_1} = \text{const} \quad (\text{does not depend on } \xi).$$

The solution to Equation (4) with initial conditions:

$$\eta(0) = 0 \quad \text{and} \quad \eta'(0) = 0$$

and with the wire tip ($\xi = b$) having point contact with the surface (then $\eta''(b) = 0$) is:

$$\eta(\xi) = \frac{c_2(\alpha)}{c_1(\alpha)} \frac{1}{\omega} [(1 - \cos \omega \xi) \tan \omega b - (\omega \xi + \sin \omega \xi)], \quad (5)$$

where:

$$\omega^2 = \frac{c_1(\alpha) F_x}{EI}.$$

The problem is intractable because:

- ω is unknown (dependent on the unknown F_x)
- and b is unknown (dependent on h or f).

In (4), we should require for $\xi = b$ to be $\eta(b) = f = h \cdot \sin \alpha$, then we obtain:

$$h \sin \alpha = \frac{c_2(\alpha)}{c_1(\alpha)} \frac{1}{\omega} [(1 - \cos \omega \xi) \tan \omega b - (\omega \xi + \sin \omega \xi)] = \eta(b).$$

Thus, after employing geometric relationships, we obtain the following equation:

$$h = \frac{c_2 d (\tan \omega b - \omega b)}{\omega b - c_2 \cos \alpha \tan \omega b}. \quad (6)$$

Condition (4) will be satisfied after employing (5), so the equation is rewritten as:

$$\eta'(\xi) = \frac{c_2}{c_1} \left[\frac{\cos \omega (b - \xi)}{\cos \omega b} - 1 \right],$$

then

$$\frac{1}{2} \int_0^b [\eta'(\xi)]^2 d\xi = \left(\frac{c_2}{2c_1} \right)^2 \left(\frac{1}{\cos^2 \omega b} - 3 \frac{\tan \omega b}{\omega b} + 2 \right) \cdot b.$$

Employing

$$b = \frac{a+r}{\sin \alpha} - r + h \cos \alpha = d + h \cos \alpha$$

we obtain:

$$1 - \frac{a+r}{\sin \alpha} + r - h \cos \alpha = \left(\frac{1}{\cos^2 \omega b} - 3 \frac{\tan \omega b}{\omega b} + 2 \right) \cdot b. \quad (7)$$

Substituting (6) for (7) we obtain a transcendental equation with the unknowns ωb . Only the lowest roots of the equation calculated as a function of α are physically feasible. These roots enable the value of ω to be calculated.

It applies to all the components of the interaction force, that is:

$$F_x = \frac{EI\omega^2}{c_1}, \quad F_y = \mu F_x,$$

$$F_{\xi} = c_1 F_x, \quad F_{\eta} = c_2 F_x,$$

as well as to the bending line for $\eta(\xi)$.

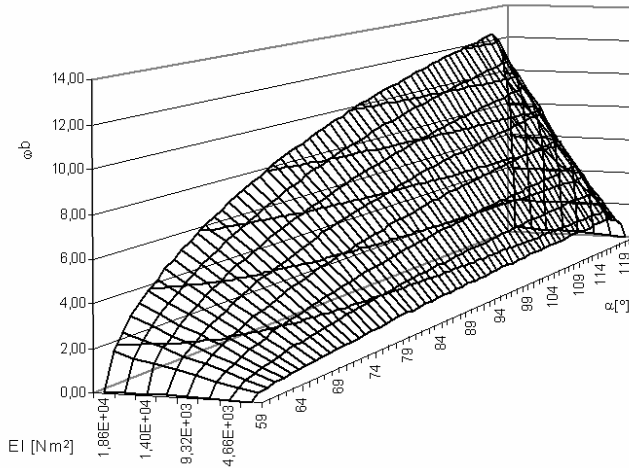


Fig. 2. Changes in the parameter ωb as a function of the rotation angle and filament flexural rigidity

Figure 2 shows the changes in the parameter ωb as a function of $\alpha = \omega_0 t$ and filament flexural rigidity EI at the following parameters: $l = 0.05$ m, $a = 0.04$ m, $r = 0.02$ m, $\mu = 0.5$.

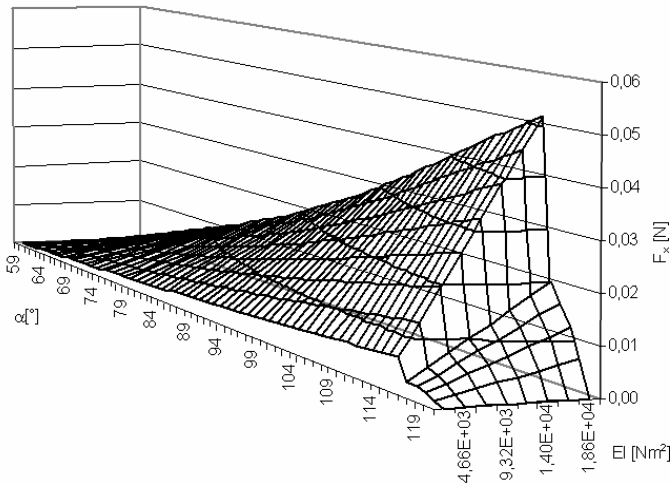


Fig. 3. The values of force component F_x , interaction with the surface as a function of rotation angle α and filament flexural rigidity EI

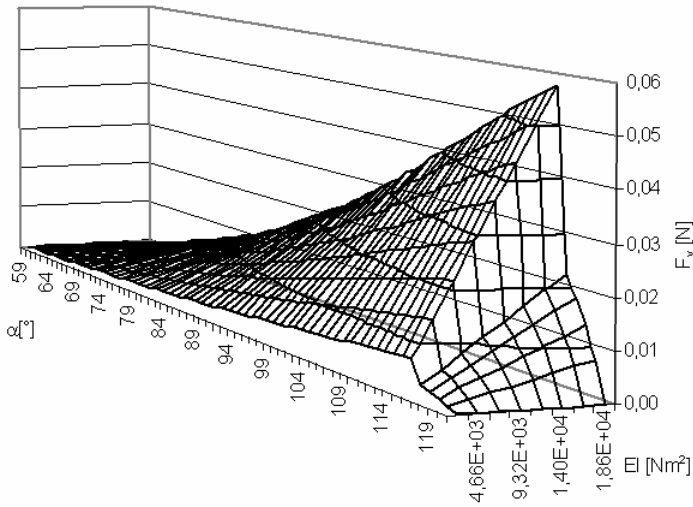


Fig. 4. The values of force component F_y , interaction with the surface as a function of rotation angle α and filament flexural rigidity EI

Graphs of the changes in the values of force components F_x , F_y as a function of the rotation angle and filament flexural rigidity EI have been presented in Figures 3–4.

Graphs of the changes in the values of force components F_ξ , F_η as a function of the rotation angle and filament flexural rigidity EI have been presented in Figures 5–6.

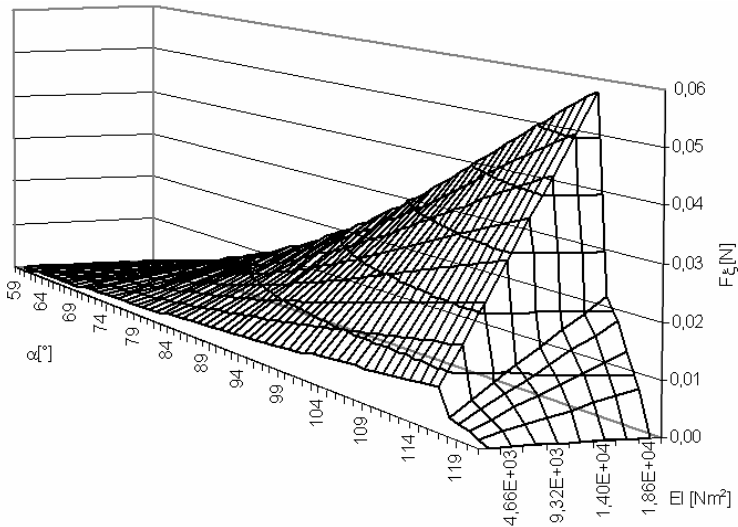


Fig. 5. The values of force component F_ξ , interaction with the surface as a function of rotation angle α and filament flexural rigidity EI

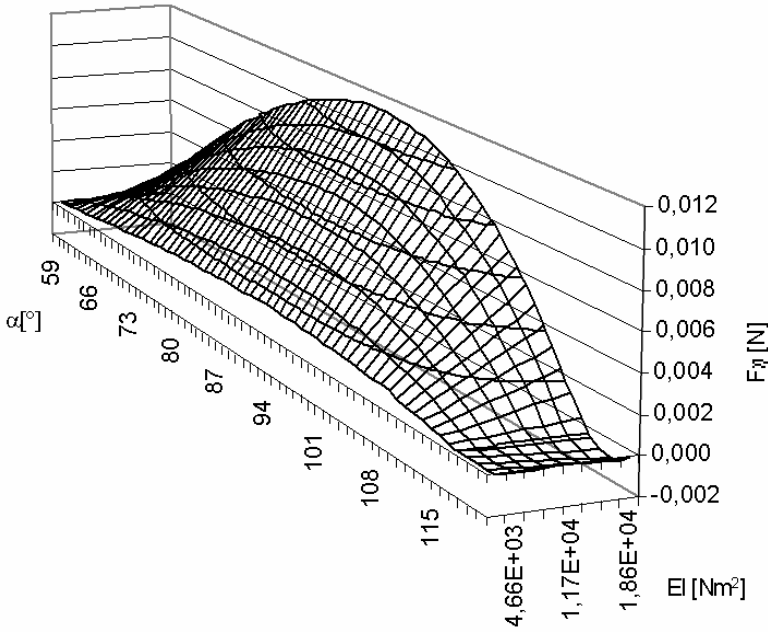


Fig. 6. The values of force component F_η interaction with the surface as a function of rotation angle α and filament flexural rigidity EI

The changes in the relationship F_η as a function of the angle $\alpha = \alpha(t)$ have to be pointed out. At $\alpha \approx 116^\circ$ the sign of the force is reversed. Consequently, the force causes the filament to straighten when it loses contact with the machined surface.

3. Dynamics of a single filament of a circular filamentary brush

The equation of the motion of a filament with its mass taken into account can be shown by coordinates $K \xi \eta$ as an equation [2] describing relative motion. We assume that $|\eta(\xi, t)| \ll 1$ and omit Coriolis inertial forces which are negligibly small in this case in order to obtain:

$$EI \frac{\partial^4 \eta}{\partial \xi^4} + F_{\xi 1} \frac{\partial^2 \eta}{\partial \xi^2} + \rho A \frac{\partial^2 \eta}{\partial t^2} = -F_{\eta 1} \delta(\xi - b) + \rho A (r + \xi) \ddot{\alpha}. \quad (8)$$

It can be shown that when inertial forces are neglected the equation can be rewritten as (3a). Forces F_ξ and F_η are marked $F_{\xi 1}$ and $F_{\eta 1}$, respectively, because these are not the same forces as in the previous expressions.

Solutions have to be looked for with boundary conditions being:

$$\left. \begin{aligned}
 &\text{for } \xi(0) = 0 \text{ we have } \eta(0, t) = 0 \text{ and } \left. \frac{\partial \eta}{\partial \xi} \right|_{\xi=0} = 0, \\
 &\text{for } \xi = b(t) \text{ we have } \left. \frac{\partial^2 \eta}{\partial \xi^2} \right|_{\xi=b(t)} = 0 \text{ and } \left[EI \frac{\partial^3 \eta}{\partial \xi^3} + F_{\xi_1} \frac{\partial \eta}{\partial \xi} \right]_{\xi=b(t)} = -F_{\eta_1}, \\
 &\text{and initial conditions:} \\
 &\eta(\xi, 0) = 0, \left. \frac{\partial \eta}{\partial t} \right|_{t=0} = 0.
 \end{aligned} \right\} (9)$$

In addition, the geometric conditions mentioned earlier have to be met as well as condition (2). This boundary-initial problem cannot be solved by conventional methods. It is very hard to obtain even approximate numerical solutions for the equation.

If we assume that the filaments maintain contact with the machined surface, the following condition is satisfied:

$$\frac{1}{2} \int_0^b [\eta'(\xi)]^2 d\xi = l - b. \quad (10)$$

It is very hard to obtain even approximate solutions for the equation.

This boundary-initial problem cannot be solved by conventional methods. Based on the solutions presented above, the Galerkin approximation was used. At $\alpha = \omega_0 t$ the last component of Equation (8) disappears.

Let us assume that the first approximation is

$$\eta(\xi, t) \approx Y(\xi) \cdot S(t), \quad (11)$$

where:

the value $S(t)$ describes the shift of the filament tip towards the axis η when is multiplied by $Y(b)$,

the function of $Y(\xi)$ has been chosen arbitrarily; it satisfies the conditions $Y(0) = 0$ and $Y'(0) = 0$ and will be integrated using the variable limits of $0 - b(t)$.

As a result we obtain an ordinary differential equation containing variable coefficients because

$$b = b(\alpha) = b(t),$$

$$m_r(b) \cdot \ddot{S}(t) + k_r(b) \cdot S(t) = -F_{\eta_1} Y(b), \quad (12)$$

where:

$$m_r = \rho A \int_0^b Y^2(\xi) d\xi,$$

$$k_r = EI \int_0^b Y^{IV}(\xi) Y(\xi) d\xi + F_{\xi 1} \int_0^b Y^{II}(\xi) Y(\xi) d\xi,$$

whose solution should satisfy condition (10). Consequently, we obtain a system of two equations with two unknowns $S(t)$ and $b(t)$.

Figure 7 shows a numerical solution for the equation describing filament tip displacement along the machined surface as a function of the angle α (being simultaneously a function of time $\alpha = \omega_0 t$) for $\rho A = 3.39 \cdot 10^{-4}$ kg/m, that is:

$$\bar{y} = (r+1) \cos \alpha_0 - \frac{r+a}{\tan \alpha} - S(t)Y(b) / \sin \alpha, \quad (13a)$$

$$\alpha_0 = \arcsin\left(\frac{r+a}{r+l}\right). \quad (13b)$$

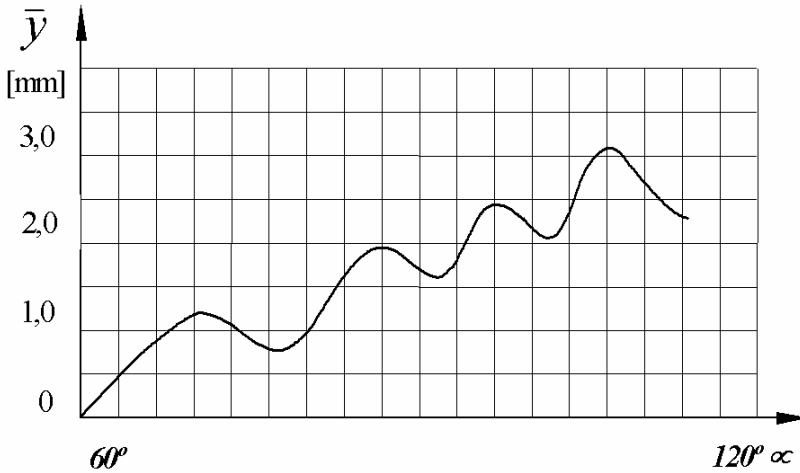


Fig. 7. Dynamic displacement of the filament tip along the line of contact with the surface as a function of the rotation angle of the disk $\alpha(t)$

Equation (13a) can be rewritten as:

$$\bar{y} = R \cos \alpha_0 - \frac{r - \Delta}{\tan \alpha} - S(t)Y(b) / \sin \alpha,$$

where:

R – the disk outside radius,

Δ – the filament radial deflection value applied.

Figure 7 shows that the movement of the filament along the machined surface is not monotonic. It demonstrates that the influence of the filament dynamics on its load can be quite considerable. The paper offers only a brief outline of the problem which requires further research.

4. Conclusions

- Lower packing densities of filament wires diminish the effect of mutual filament support, thus making the brush more deformation-prone. It makes it possible to adjust the deflection (Δ) parameter within a wider range of settings, with the disk retaining its original size.

- The pressure force the filament tip exerts on the surface along the displacement path increases in a non-linear manner, with its value suddenly dropping towards the end of the displacement path.

- Upon analysis of the differential equation of a single filament displacement path it can be stated that:

- changes of the force of the filament interactions with the surface are directly proportional to the changes of the filament stiffness, thus a solution for $(EI)_1$ is also applicable to $(EI)_2$,

- the shapes of the bending line are identical if for a given position of a workpart (specified by the angle α) the values of interaction forces $(F(\alpha)i)$ are proportional to the corresponding stiffness values of the elements $(EI)_i$.

References

- [1] Duwell E.J., Bloecher U.: *Deburring and Surface Conditioning with Brushes Made with Abrasive Loaded Nylon Fiber*, Society of Manufacturing Engineers, Technical Paper MR83-684, Dearborn, MI. 1983.
- [2] Gutowski R., Swietlicki W. A.: *Dynamika i drgania układów mechanicznych*, PWN, Warszawa, 1986.
- [3] Nowicki B., Spadło S.: *Smoothing the surface by brush electrodischarge mechanical machining – BEDMM*, Central European Exchange Program for University Studies Project PL-1- CEEPUS, Science Report, Kielce, 1998, pp. 129–137.
- [4] Spadło S.: *Complex Shape Surface Finishing Process*, Patent PL 172559, 1997.

- [5] Nowicki B., Pierzynowski R., Spadło S.: *New Possibilities of Machining and Electrodischarge Alloying of Free-Form Surfaces*, Journal of Materials Processing Technology, 2001, Vol. 109, No. 3, pp. 371–376.
- [6] Nowicki B., Pierzynowski R., Spadło S.: *The Superficial Layer of Parts Machined by Brush Electrodischarge Mechanical Machining (BEDMM)*, Proceedings of II International Conference on Advances in Production Engineering. Part II, Warsaw, June, 2001, pp. 229–236.
- [7] Spadło S.: *Experimental Investigations of the Brush Electrodischarge Mechanical Machining Process – BEDMM*, Advances in Manufacturing Science and Technology, Quarterly of the Polish Academy of Sciences, 2001, Vol. 25, No. 3, pp. 117–135.
- [8] Osiecki J., Spadło S.: *A model of mechanical interactions of a brush electrode with a flat surface*, Proc. of 9th Int. Sci. Conf. on Production Engineering, Computer Integrated Manufacturing and High Speed Machining, Croatian Association of Production Engineering, Lumbarda, 2003, pp. IV066–IV072.
- [9] Timoshenko S.P., Gere J.M.: *Theory of Elastic Stability*, second edition, McGraw-Hill, Inc., London, 1961, pp. 76–81.
- [10] Wick C., Veilleux R.F.: *Mechanical and Abrasive Deburring and Finishing*, SME Tool and Manufacturing Engineers Handbook, Chapter 16, Vol. 3, 1985.

Analiza charakterystyk narzędzi szczotkowych

Przedstawiono analityczne rozwiązanie zagadnienia sił, z jakimi oddziałują pojedyncze włókna szczotki obrotowej z powierzchnią. Przeprowadzono analizę deformacji pojedynczych drucików szczotki, uwzględniając występujące więzy kinematyczne dla przypadku powierzchni płaskiej niepodatnej z występowaniem tarcia. Przedstawiono wyniki symulacji komputerowych w postaci zależności sił oddziaływań drucików z powierzchnią w funkcji kąta obrotu szczotki.

Full-scale laboratory tests and FEM analysis of corrugated steel culverts under standardized railway load

B. KUNECKI, E. KUBICA

Wrocław University of Technology, Wybrzeże Wyspiańskiego 25, 50-370 Wrocław

This paper describes a full-scale static test conducted on a corrugated steel culvert with 2.99 m span and 2.40 m in height. The test was carried out in the Bridge and Road Research Institute, Wrocław Branch, Poland, in 1998 for a Norwegian producer of culverts. The standardized railway load configuration UIC 71 for Europe was applied at various soil cover (from 0.3 m to 1.0 m). Several full-scale tests have been performed in the field to validate the long-term performance and great load bearing capacity of these structures, but few structures have been tested in controlled conditions in a test facility like the test in Poland. In order to verify the test results, a finite element model for the structures tested was constructed. The empirical results obtained were compared with results obtained by means of the Finite Elements Method (FEM). To perform the FEM analysis Cosmos/M system software was used. Only results obtained at 0.8 m soil cover were presented and compared.

Keywords: *steel culverts, FEM, instrumentation, full-scale test*

1. Introduction

Corrugated steel culverts are increasingly being used in road and railway projects as an alternative solution to concrete bridges and culverts. Their construction period is short, and the structures have both technical and economical advantages. Several full-scale tests have been carried out in the field to validate the long-term performance and load bearing capacity of these structures [4, 9]. In contrast to that, only few tests of life-size structures have been performed under fully controlled laboratory conditions.

The experimental data obtained under such conditions are needed in order to verify software tools used for numerical analysis as well as to help us to optimize and design more economic structures. This is of the first importance having high-quality test results when designing flexible, long-span buried structures with minimum cover for live railway and road loads.

2. Description of the structure tested

The structure tested was located in the test stand which is shown in Figure 1. The test stand has the form of an 80 m long and 12 m wide reinforced concrete foundation with a system of anchors and a steel frame serving as a support structure for the system of two hydraulic servos with a modern control and feeding system ensuring full control over the static and dynamic loads in real time. The culvert tested had

a span of 2.99 m, a height of 2.40 m and a length of 14.4 m. Soil cover of 0.80 m was used while standardising railway loads. The steel material was of FE 360 B FN quality to meet European Standard EN 10025. The minimum yield stress was 245 MPa. The corrugation was 150×50 mm and the steel thickness was 3.75 mm [2]. The steel plates were joined by the bolts, 20 mm in diameter, with minimum tensile strength of 830 MPa. The bolts and the joint are shown in Figure 2, and the properties of steel plate are listed in Table 1.



Fig. 1. View of the culvert tested

Table 1. Properties of steel plate

| Plate thickness [mm] | Area A [mm ² /mm] | Moment of inertia I [mm ⁴ /mm] | Section modulus W [mm ³ /mm] | Radius of gyration i [mm] |
|----------------------|--------------------------------|---|---|-----------------------------|
| 3.75 | 4.72 | 1479.8 | 55.1 | 17.7 |

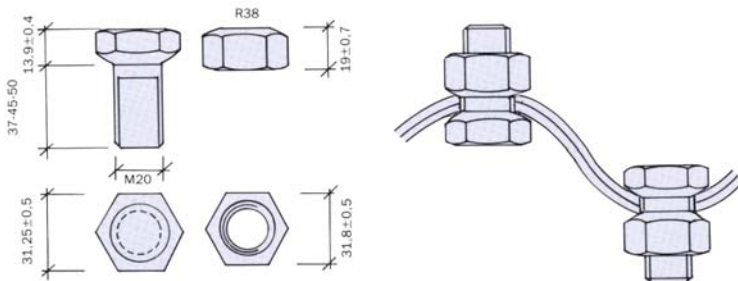


Fig. 2. Cross-section of the steel plate and the bolts

The test bin was 12 m long, 5 m wide and 4 m high. It was constructed from railway sleepers and steel beams. The test bin was backfilled with a well-graded material with maximum grain size of 32 mm. The backfill was placed in layers with maximum thickness of 20 cm before compaction. The required degree of compaction was 97% Standard Proctor, expected for the 500 mm closest to the structure, where 94% Standard Proctor was sufficient. The cross-section of the test stand is shown in Figure 3.

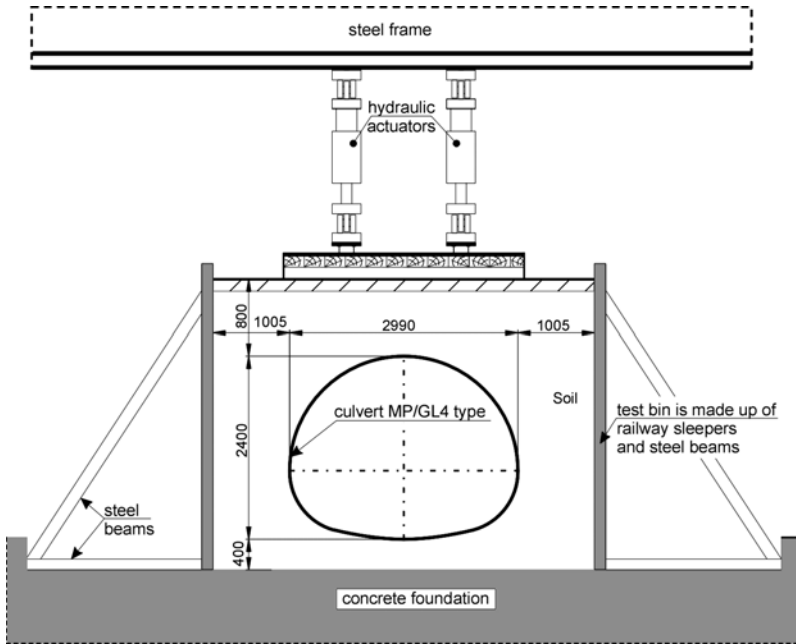


Fig. 3. Cross-section of the culvert tested

3. Loads

The loads from two hydraulic actuators were distributed through two layers of wooden sleepers and 20 mm thick steel plate with area of $2.60 \text{ m} \times 3.15 \text{ m}$. The cross-section and view of load distribution system are shown in Figure 4.

The standardised configuration of railway loads UIC 71 for Europe was applied. Due to the distribution effect of rails, sleepers and ballast bed, the axle loads from the locomotive ($4 \times 250 \text{ kN}$) produce a uniform area load which equals approx. 52.0 kN/m^2 at a base of the ballast bed at a depth of 0.5 m. At a depth of 0.8 m the area load is 51.0 kN/m^2 . The dynamic load factor (European Standard) is 1.37 according to the formula with 0.8 m cover. The resulting pressure which was used in railway standard static test equalled $51.0 \times 1.37 = 69.87 \text{ kN/m}^2$. A real force used in each actuator is listed in Table 2. Three standard static loads were applied at regular time intervals (about 20 minutes).

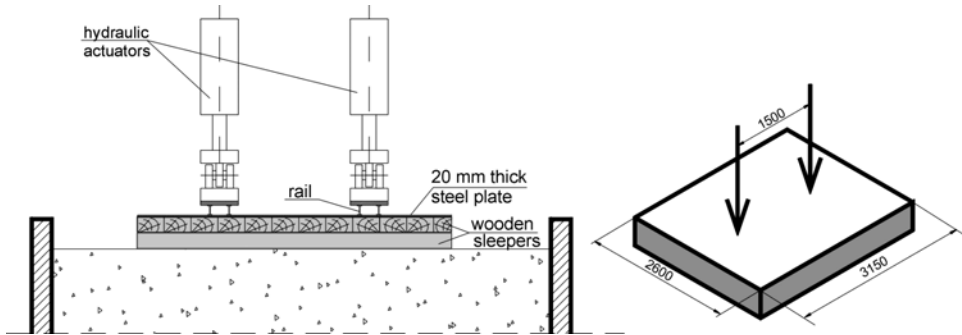


Fig. 4. Cross-section and view of load distribution system

Table 2. Loads

| Number of loads [-] | Soil cover h [m] | Dynamic factor ϕ [-] | Area of rigid plate [m ²] | Total force for two actuators F [kN] | Total pressure p [kN/m ²] |
|------------------------|-----------------------|------------------------------|--|---|--|
| 3 | 0.8 | 1.37 | 8.19 | 572 | 69.84 |

4. Instrumentation and measurement

The instrumentation comprised the following: strain gauges on the inside of metal culvert allowing axial and bending strains to be measured; earth pressure cells allowing a total stress in the soil to be measured; displacement gauges inside culverts. A detailed description of instrumentation is presented below.

4.1. Strain gauges

Strain gauges were placed at 14 locations inside the steel structure. Two gauges were fitted to each location, one at the top of the corrugation and one at the bottom (total 28 strain gauges). The location of all strain gauges is shown in Figure 5a. This configuration allowed axial and bending strains to be measured. Dummy gauges were installed to provide temperature compensation. Electroresistant strain gauges of the Hottinger Baldwin Masstechnik 6/120LY41 type were installed. Strain gauges had 6 mm measuring base, resistance of 120 Ω and factor k equal to 2.02. The measurements were performed with the use of the tension-metric bridge UPM 100 also from the Hottinger Baldwin Masstechnik. The UPM 100 was connected to Macintosh computer equipped with “Beam” software.

4.2. Earth pressure cells

Earth pressure around steel structure was measured by earth pressure cells. In order to specify the pressure in the surroundings of culvert, ten earth pressure cells were installed in the soil. Eight of them were installed at steel structures, about 6 cm from

steel plates. Additionally two earth pressure cells were installed on the top of both sides of the structure at a distance of 1.5 m from symmetry axis. The location of all earth pressure cells is shown in Figure 5b. Each cell is sheltered by 0.03 m layer of dry sand and durable foil. View of earth pressure cells during installation is shown in Figure 6. Magnetoelastic pressure cells from Wrocław University of Technology were used. Measure system PPN-3 with “Dynusing” software was used for data collecting from gauges.

4.3. Displacement gauges

Three displacement gauges were installed in the same plane (one vertical gauge and two horizontal gauges). The displacement gauges allow a relative displacement of the metal culvert to be measured. The maximum vertical and horizontal diameters were measured by displacement gauges. The W50TS type inductive gauges were used from the Hottinger Baldwin Masstechnik. Each gauge had a measurement range of ± 50 mm and precision class of 0.4. The locations of all displacement gauges are shown in Figure 5a.

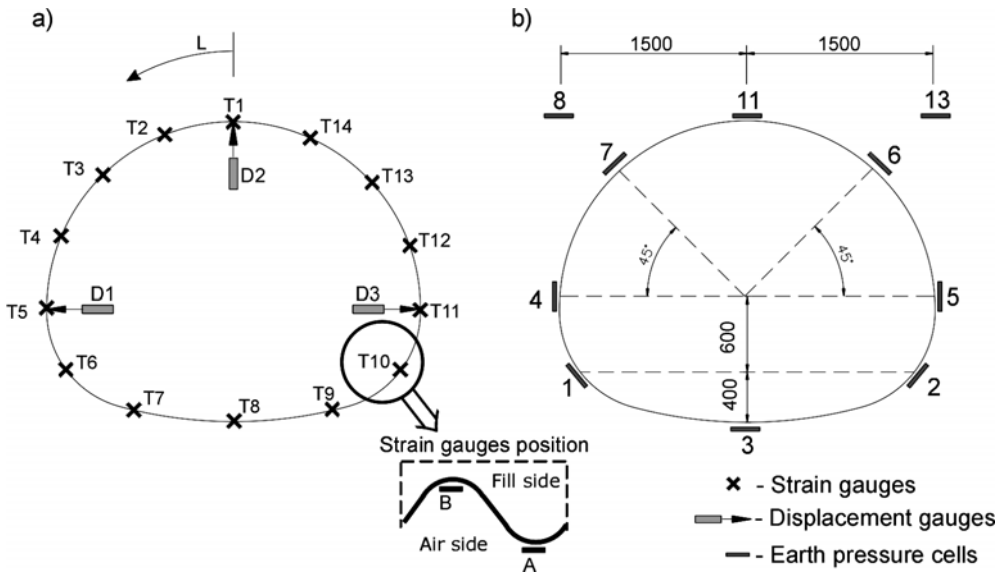


Fig. 5. Instrumentation of the culvert tested:
a) strain and displacement gauges, b) earth pressure cells

After each load strain gauges, earth pressure cells and displacement gauges were reset.



Fig. 6. View of earth pressure cells during installation

5. Test results

All test results from displacement, earth pressure and strain gauges are listed in Tables 3, 4, 5. There are shown the values from three loads and average value. All of them were obtained 20 s after reaching a full load assumed.

The stresses in steel structure were calculated based on strains taking into consideration that the elastic modulus of steel is $E_s = 205$ GPa. The stresses at each measurement point (two of strain gauges) were allocated to axial stresses and bending stresses according to the known equations:

$$\sigma_a = \frac{\sigma_A + \sigma_B}{2}, \quad (1)$$

$$\sigma_b = \frac{\sigma_A - \sigma_B}{2}, \quad (2)$$

where:

- σ_a – axial stresses,
- σ_b – bending stresses,
- σ_A – stresses in the point A (at the crest of corrugation),
- σ_B – stresses in the point B (at the valley of corrugation).

Table 3. Displacement [mm]

| Gauges | D1 (left) | D2 (top) | D3 (right) |
|----------|-----------|----------|------------|
| Load I | 1.16 | -2.55 | 1.12 |
| Load II | 0.85 | -2.24 | 1.00 |
| Load III | 0.83 | -2.19 | 0.98 |
| Average | 0.95 | -2.33 | 1.03 |

Table 4. Earth pressure [kPa]

| Gauges | 1 | 2 | 3 | 4 | 5 | 6 | 7 | 8 | 11 | 13 |
|----------|------|------|-----|------|------|------|------|------|------|------|
| Load I | 57.2 | 56.4 | 0.1 | 32.2 | 27.0 | 22.2 | 27.4 | 32.6 | 29.1 | 50.2 |
| Load II | 51.2 | 49.8 | 0.1 | 31.9 | 27.4 | 21.1 | 26.4 | 31.3 | 25.8 | 50.7 |
| Load III | 49.8 | 48.7 | 0.1 | 32.1 | 27.0 | 20.9 | 26.1 | 30.9 | 25.3 | 50.1 |
| Average | 52.7 | 51.6 | 0.1 | 32.1 | 27.1 | 21.4 | 26.6 | 31.6 | 26.7 | 50.3 |

Table 5. Axial stress (N) and bending stress (M) [kPa]

| Gauges | Load I | | Load II | | Load III | | Average | |
|--------|---------|--------|---------|--------|----------|--------|---------|--------|
| | N | M | N | M | N | M | N | M |
| T1 | -5.806 | 0.122 | -5.947 | 0.092 | -5.947 | 0.092 | -5.900 | 0.102 |
| T2 | -2.903 | 0.058 | -3.398 | 0.055 | -3.398 | 0.056 | -3.233 | 0.056 |
| T3 | -9.275 | -0.119 | -9.487 | -0.111 | -9.416 | -0.116 | -9.393 | -0.115 |
| T4 | -10.054 | -0.062 | -10.054 | -0.050 | -9.841 | -0.051 | -9.983 | -0.054 |
| T5 | -6.868 | -0.099 | -6.655 | -0.092 | -6.584 | -0.088 | -6.702 | -0.093 |
| T6 | 0.425 | 0.131 | 0.354 | 0.114 | 0.354 | 0.114 | 0.378 | 0.120 |
| T7 | -0.354 | 0.011 | -0.496 | 0.009 | -0.354 | 0.009 | -0.401 | 0.010 |
| T8 | -0.425 | -0.002 | -0.425 | -0.003 | -0.496 | -0.001 | -0.448 | -0.002 |
| T9 | 0.354 | 0.012 | -0.354 | 0.011 | -0.354 | 0.012 | -0.118 | 0.012 |
| T10 | -0.071 | 0.131 | -0.283 | 0.113 | -0.142 | 0.115 | -0.165 | 0.120 |
| T11 | -8.142 | -0.115 | -7.788 | -0.106 | -7.717 | -0.102 | -7.882 | -0.108 |
| T12 | -11.257 | -0.080 | -10.903 | -0.063 | -10.832 | -0.064 | -10.998 | -0.069 |
| T13 | -11.186 | 0.124 | 11.045 | -0.129 | -10.903 | -0.135 | -3.682 | -0.047 |
| T14 | -7.151 | 0.078 | 7.292 | 0.087 | -7.080 | 0.093 | -2.313 | 0.086 |

6. Modelling of the structure

Analyses of the soil–structure system were carried out using the computer software Cosmos/M system. The computer software allows the simulation of live loads only. The Cosmos/M software allows the simulation of live loads together with deadweight of soil and structures as well.

The finite elements and static model of soil–structure system is shown in Figure 7. Only half of the system was modelled, as the geometry and loading were essentially symmetric. The culvert structured was modelled by 32 Beam2D elements, and the soil by 316 Plane2D elements.

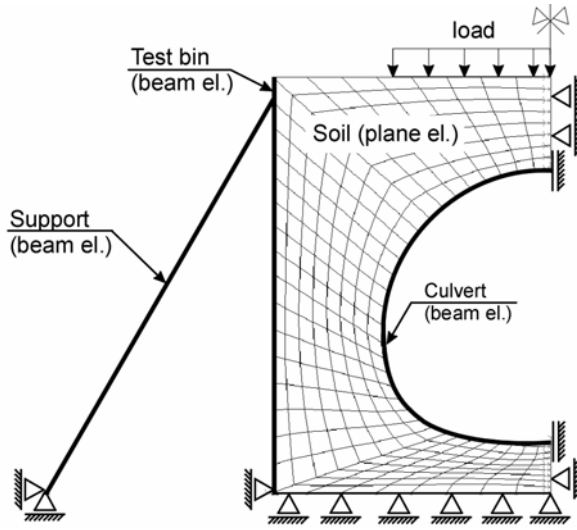


Fig. 7. Finite element modelling of culvert, soil and test bin

6.1. Element Beam2D

Beam2D is a 2-node uniaxial element for two-dimensional structural. The element has three degrees of freedom (two translations and one rotation) per node for structural analysis. All elements have to be defined in the X - Y plane as shown in Figure 8. Output results are the following: forces, moments, and stresses are available in the element coordinate system.

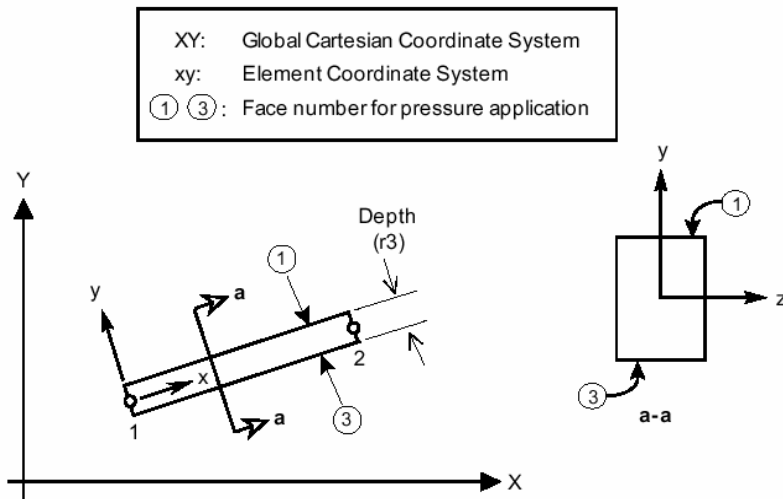


Fig. 8. Beam2D element

Real constants used in Beam2D element are: $r1$ – cross-sectional area (A), $r2$ – moment of inertia (Jx), EX – modulus of elasticity in the 1st material direction, $NUXY$ – Poisson’s ratio relating the 1st and 2nd material directions, $DENS$ – density.

6.2. Element Plane2D

Plane2D is a 4- to 8-node two-dimensional element for plane stress, plane strain, or axisymmetric structural with symmetric and non-symmetric (asymmetric) loading. All elements have to be defined in the X – Y plane. Only two translational degrees of freedom per node are considered for structural analysis. The nodal input pattern is shown in Figure 9 for an 8-node element illustrating its local node numbering. The element however can be used with 4- to 8-nodes by assigning zeros (0) at the locations of missing nodes during element connectivity definition. Triangular in shape elements can also be considered. In this case, the third and the fourth nodes (in case of 4-node elements) and the third, the fourth and the seventh nodes (in case of 5- to 8-node elements) will be assigned the same global node number as shown in Figure 9.

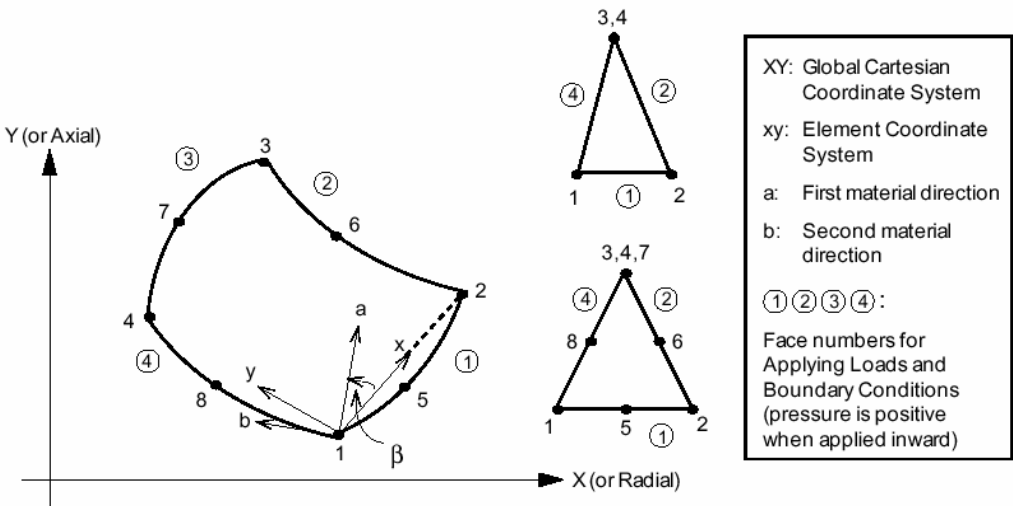


Fig. 9. Plane2D element

Real constants used in Plane2D element are: $r1$ – thickness, EX – modulus of elasticity in the 1st material direction, $NUXY$ – Poisson’s ratio relating the 1st and 2nd material directions, $DENS$ – density, $FRCANG$ – angle of internal friction.

7. FEM analysis results

The measured and computed bending stresses (M) distributed in the steel structure are shown in Figure 10. The distributions are seen to be in a close agreement.

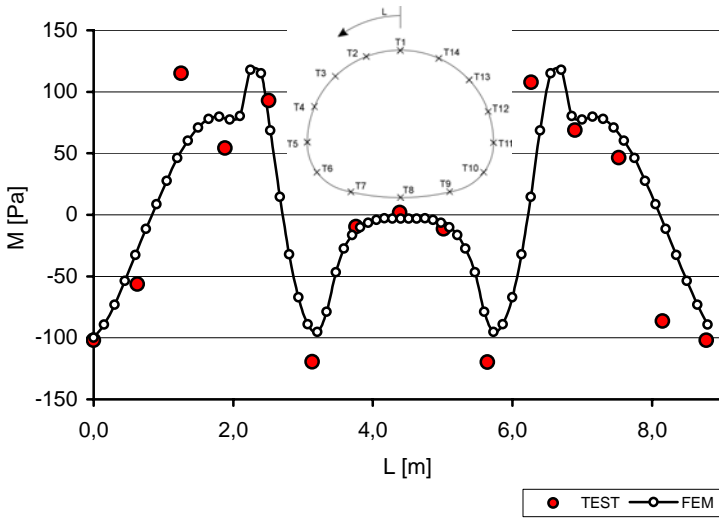


Fig. 10. Distribution of bending stresses (M)

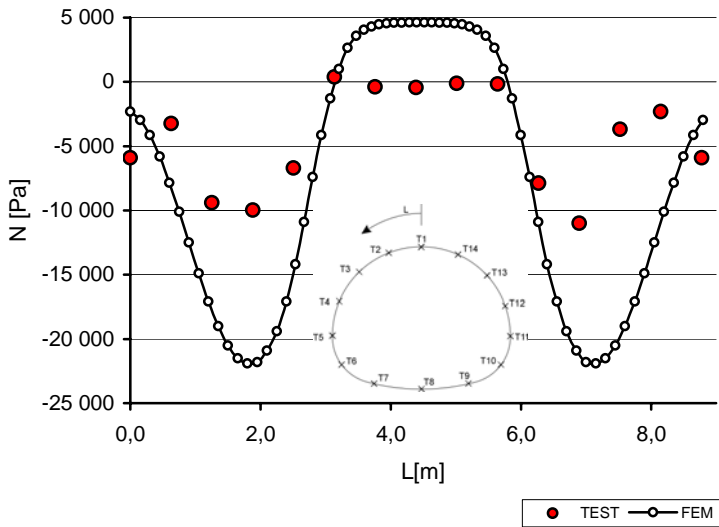


Fig. 11. Distribution of axial stresses (N)

The measured and computed axial stresses (N) distributed in the steel structure are shown in Figure 11. The axial stresses predicted are not in a good agreement with the values measured, being significantly higher.

The measured and computed displacements in the steel structure are listed in Table 6. The displacements in selected points are seen to be in a close agreement. The difference between test and FEM analysis is 0.11 mm in the case of vertical displacement and 0.08 mm in the case of horizontal displacements (gauges No. D3).

Table 6. Comparison of displacement in selected points [mm]

| Point | D1 | D2 | D3 |
|-------|------|-------|------|
| Test | 0.95 | -2.33 | 1.03 |
| FEM | 0.95 | -2.22 | 0.95 |

The measured and computed earth pressures in the soil are listed in Table 7. The earth pressures in selected points are seen to be in a close agreement.

Table 7. Comparison of earth pressure [kPa]

| Point | 1 | 2 | 3 | 4 | 5 | 6 | 7 | 8 | 11 | 13 |
|-------|-------|-------|-----|------|------|------|------|------|------|------|
| Test | 52.7 | 51.6 | 0.1 | 32.1 | 27.1 | 21.4 | 26.6 | 31.6 | 26.7 | 50.3 |
| FEM | 108.7 | 108.7 | 0.0 | 58.8 | 58.8 | 88.4 | 88.4 | 65.6 | 26.6 | 65.6 |

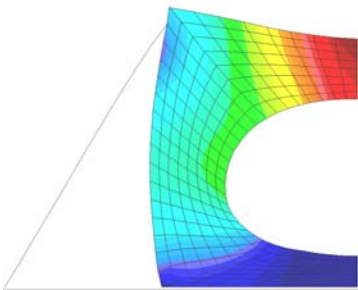


Fig. 12. Displacement

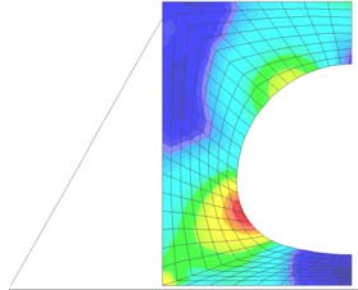


Fig. 13. Von Mises

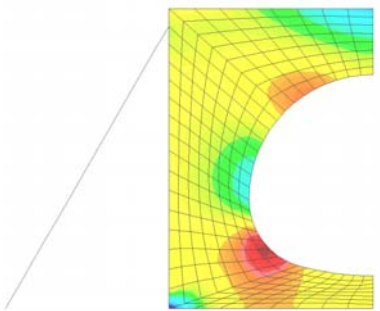


Fig. 14. Sigma X

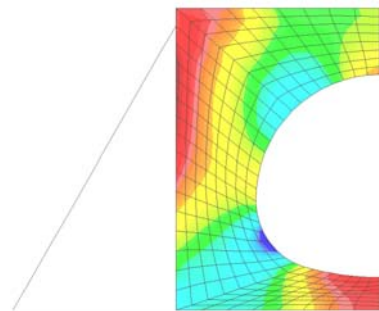


Fig. 15. Sigma Y

Cosmos/M system allows us to present several results in graphical form. Displacement distribution and deformation are shown in Figure 12. Normal stresses in the x -direction are presented in Figure 14, and normal stresses in the y -direction are shown in Figure 15. The von Mises stress (σ_{von}) component is calculated from the stress components as shown below [7]:

$$\sigma_{\text{von}} = \sqrt{\frac{1}{2}[(\sigma_x - \sigma_y)^2 + (\sigma_x - \sigma_z)^2 + (\sigma_y - \sigma_z)^2 + 3(\tau_{xy}^2 + \tau_{xz}^2 + \tau_{yz}^2)]}, \quad (3)$$

where:

σ_i – normal stresses (i – the x, y, z directions),

τ_{xy} – shear stress in the x - y plane,

τ_{xz} – shear stress in the x - z plane,

τ_{yz} – shear stress in the y - z plane.

8. Conclusion

The comparative study indicates that the numerical culvert's displacements and empirical measurements are almost equal. This means that a stiffness of whole soil-structure system and the finite elements for to modelling were wisely selected. The same correspondence appeared in the case of bending stresses in steel structure.

The axial stresses in the structure are not in a good agreement with numerical and empirical values. The numerical values are significantly higher. Numerical modelling of contact surface between steel shell and soil should be changed. The solution to the problem would be using contact elements like GAP type or applying a springs with specific stiffness between soil and structure.

Stiffness of retaining walls significantly influences distribution of stresses in soil and culvert structure as well (both qualitative and quantitative).

References

- [1] Kunecki B., Kubica E.: *Experimental identification of load distribution in steel culverts*, Research report no. 81/30, pp. 103, Wrocław University of Technology, Institute of Building Engineering, Wrocław, 2002.
- [2] Kunecki B. et al.: *Report from the investigation on the Multiplate culverts and Helcore and DV/Optima tubes*, Report no. IBDiM-TW 26999/W-374, Road and Bridge Research Institute, Wrocław, 1999.
- [3] Korusiewicz L., Kunecki B.: *Experimental and numerical analysis of internal forces in steel culverts of the multiplate type*, The 7th International Conference "Shell Structures, Theory and Application" Gdańsk, October 2002, pp. 137.
- [4] Vaslestad J.: *Long-term behaviour of flexible large-span culverts*, Publication no. 74, Norwegian Public Road Administration, Oslo, 1994, pp. 33.

- [5] Vaslestad J.: *Soil structures interaction of buried culverts*, Department of Civil Engineering, the Norwegian Institute of Technology, 1990.
- [6] Vaslestad J., Madaj A., Janusz L., Bednarek B.: *Field measurements of an old brick culvert sliplined with a corrugated steel culvert*, Transportation Research Board, Washington, 2004.
- [7] Rusiński E.: *Finite Elements Method – Cosmos/M system*, Publication of Transport and Communication, Warsaw, 1994.
- [8] Konderla P., Kasprzak T.: *Computer methods in elasticity theory*. Part one. *Finite Elements Method*, Dolnośląskie Wydawnictwo Edukacyjne, Wrocław, 1997.
- [9] Byrne P.M., Srithar T., Kern C.B.: *Field measurements and analysis of large-diameter flexible culvert*, Canadian Geotechnical Journal, 1993, Vol. 30, Canada.
- [10] Polish Standard: PN-88/ B-02014 – Action on building structures – Soil loading.
- [11] Polish Standard: PN-81/ B-03020 – Building soils – Foundation bases. Static calculation and design.
- [12] *Multipel Trummo*: Catalog - AROT ViaCon.

Laboratoryjne badania w pełnej skali i analiza MES stalowych przepustów z blachy falistej pod normowym obciążeniem kolejowym

W roku 1998 w Instytucie Badawczym Dróg i Mostów, Filia Wrocław, przeprowadzono pełnowymiarowe badania modelowe przepustu typu GL4 wykonanego w technologii *multi-plate*. Przedmiotowe badania zrealizowano na zlecenie norweskiego producenta przepustów firmy ViaCon, który dostarczył materiał do badań. Zaprezentowano sposób zamontowania konstrukcji na specjalnie przygotowanym stanowisku badawczym. Podczas badań wykonano wiele obciążeń statycznych oraz dynamicznych, którym towarzyszył pomiar takich wielkości fizycznych jak: odkształcenia, przemieszczenia i napór gruntu na powierzchnie przepustu w charakterystycznych punktach konstrukcji. Przedstawiono sposób montażu czujników naporu gruntu (presjometrów) wokół powłoki przepustu.

Normowe obciążenie kolejowe (według normy europejskiej UIC 71) zostało zamodelowane przez zastosowanie sztywnej płyty przenoszącej obciążenia z siłowników na grunt.

Badania przeprowadzono dla różnych wysokości naziomu (1,0 m; 0,8 m; 0,6 m; 0,3 m). Ze względu na dużą ilość otrzymanych wyników zaprezentowano jedynie wyniki dla naziomu 0,8 m otrzymane przy obciążeniu statycznym.

Używając programu Cosmos/M, stworzono model numeryczny stanowiska badawczego i konstrukcji przepustu. Na wykresach i w tabelach porównano wyniki empiryczne z wynikami otrzymanymi metodą elementów skończonych.

Z analiz porównawczych wynika zadawalająca zbieżność ugięć powłoki przepustu. Oznacza to, że sztywności całego układu grunt–przepust oraz rodzaje użytych elementów zostały właściwie dobrane. Równie zbieżny jest rozkład naprężeń zginających w powłoce przepustu. Naprężenia ściskające mierzone na powierzchni przepustu zachowują jedynie charakter rozkładu wyznaczonego numerycznie. Należy zastanowić się nad innym sposobem zamodelowania powierzchni kontaktu między gruntem a powłoką przepustu. Sugeruje się zastosowanie elementów kontaktowych (np. typu GAP) lub zastosowanie między przepustem a gruntem sprężyn o określonej sztywności.

Zauważono bardzo duży wpływ sztywności ścian oporowych na jakościowy i ilościowy rozkład naprężeń zarówno w gruncie, jak i w powłoce przepustu.

Application of fuzzy sets to determining non-monotone behaviour of the tool life

M. MIERNIK

Wrocław University of Technology, Wybrzeże Wyspiańskiego 27, 50-370 Wrocław

The article is an attempt at showing how the theory of fuzzy sets may be used in explaining non-monotone behaviour of the tool-life function. The results obtained in orthogonal turning of Stellite cobalt alloys served as a basis for presenting rules underlying the so-called areas of undetermined chip formation and for determining local extrema of the function. The fuzzy set theory is presented to the extent that is capable of explaining the observed bifurcation between two branches of the function.

Keywords: *cutting, cobalt alloys, tool wear, fuzzy sets*

1. Non-monotone behaviour of the tool-life function

Among many factors affecting the tool life, the cutting speed is the most important. The well-known formula established firstly by Taylor [1] in 1907 states that

$$T = \frac{C_t}{v_c^s}, \quad (1)$$

where T is the time that is needed to develop a flank wear land of certain dimensions, C_t is the so-called material constant, v_c is the cutting speed and s is an experimentally determined exponent dependent on cutting conditions.

Equation (1) gives T as a globally monotone hyperbolic function of the cutting speed v_c . Precise studies performed by Podurayev [2] have shown, however, that T becomes a non-monotone function of v_c for higher cutting speeds. The phenomenon has been observed in cutting difficult-to-machine materials as well as steels.

Many attempts have been made to find such a generalized relationship $T = f(v_c)$ that would be in a full agreement with physical features of the edge wear process. No such function has been found until now for an arbitrary combination of the tool and the part materials and the wide range of cutting speed.

The non-monotone property of the $T = f(v_c)$ relationship is frequently shown as in Figure 1. The Taylor formula (1) is then considered as generally valid but particular segments of the graph have different values of constant C_t and exponent s . According to Podurayev, discontinuities in the C_t and s are due to some abrupt changes in the machining capabilities of tools involved.

Krobacher and Merchant [3] proposed the tool life to be dependent not only on the C_t value but also on the normal force F_N and temperature Θ_s obtained at the tool-workpiece interface:

$$T = \sqrt{C_t F_N \Theta_s} . \quad (2)$$

Both F_N and Θ_s depend directly on the cutting speed. Formula (2) was derived for titanium alloys cut with carbide tools, where the $T = f(v_c)$ function has long been observed to be non-monotone.

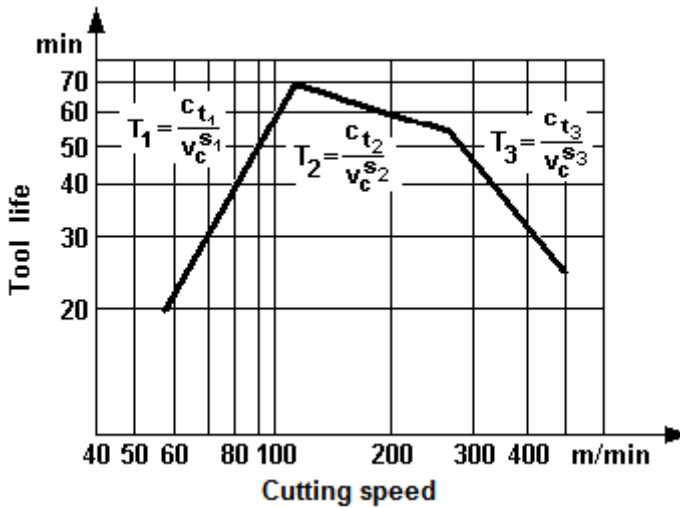


Fig. 1. Experimental dependence of tool life upon cutting speed for EI388 steel [2]

Investigations carried out by De Almeida & Hinds [4] and Miernik [5, 6] have shown, however, that formula (2) fails to deliver sound estimates in cutting Stellite cobalt alloys, if either the segmented or the saw-tooth type chips are produced. The tool-life time determined from (2) differs in such cases by up to 40% from that found experimentally.

2. Relation between chip type and non-monotone properties of the tool-life function

The studies of actual chip formation (see e.g. [5]) have shown that under different metal-cutting conditions various types of chips may be formed such as segmented, continuous or shear-localized chip. Figure 2 shows areas of basic chip types in the (v_c, γ_0) plot (γ_0 – orthogonal rake angle) in orthogonal cutting of Celsit SN cobalt alloy ($C =$

2.1%, Co = 56%, W = 14%, Cr = 25%; HRC = 51–54). The areas occupied by a given chip type do not have the borders clearly defined. Even under fixed cutting conditions the border areas must be regarded as those where mechanics of chip formation is somehow disturbed, which in turn finds its reflection in dependent variables of the cutting process being abruptly changed. Those sets of cutting conditions which give rise to abnormal chip formation have been termed as “areas of undetermined chip formation” (AUCF) and may be considered to be fuzzy sets. This is why the basic chip types in Figure 2 are separated not by lines but by hatched zones of non-zero width.

Various cutting indexes such as shear angle Φ , shear strain γ_{sh} and shear strain rate $\dot{\gamma}_{sh}$ or normal pressure δ_N acting on the edge have been found to exhibit irregular behaviour within the AUCF, and derivatives of those indexes with respect to the shear angle have been shown to be functions with singularities [7].

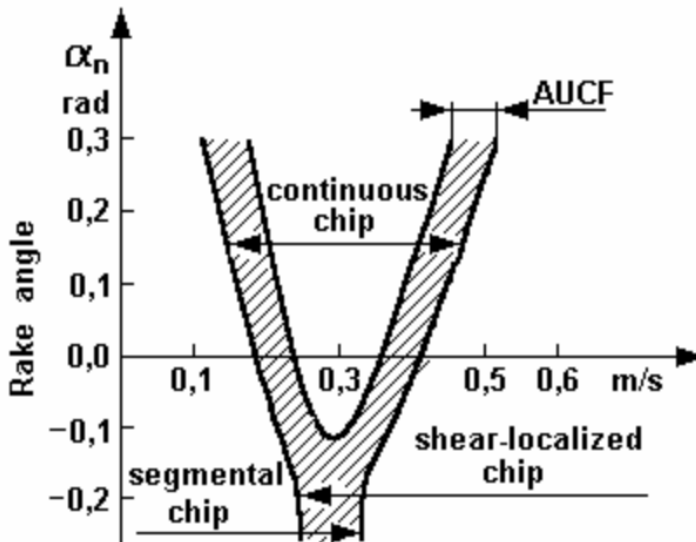


Fig. 2. Areas of occurrence of basic chip forms in cutting Celsit SN cobalt alloy [5]

The AUCF have no clearly defined borders since actual materials deviate significantly from the ideal model of thermomechanical medium because of their crystalline microstructure, lattice defects, anisotropy of thermoplastic properties, etc. The greater the scatter of local metal properties, the broader the AUCF. Another factor providing the AUCF occurrence are elastic deformations of the tool and machine structure. With all the above arguments gathered, we can say that under AUCF conditions it is impossible to formulate definite estimates of the workpiece material machinability or of the tool performance. The available experimental evidence obtained in AUCF machining tests is typical of fuzzy sets.

Analysis of the tool wear process, occurring in cutting cobalt alloys with carbide tools, revealed that the normal pressure exerted on the tool face produced by the segmented or shear-localized chips acts not on all the contact area but only on its fraction equal to the thickness of the chip segment [4, 5].

Measurements of cutting forces and characteristic dimensions of the above forms of chip served as a basis for determining actual values of normal pressure δ_N acting on the rake face. Results of the analysis (presented in Figure 3) were also used to derive the following modified version of Equation (2):

$$T = \sqrt{C_T \delta_N \Theta_N} . \quad (3)$$

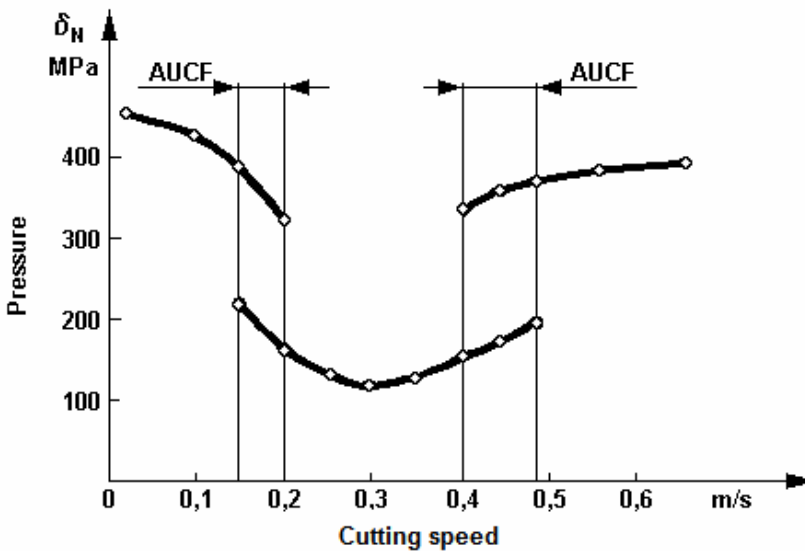


Fig. 3. Sudden changes in the value of pressure acting on the rake face [5]

Investigations carried out in study [6] were used for deriving statistically a function $T = f(v_c)$ for the Celsit SN cobalt alloy. The function turned out to be non-monotone with two local maxima (Figure 4) which occurred for the cutting speed ranges corresponding to the transition between particular chip types.

The above results contradict the Podurayev hypothesis concerning the non-monotone behaviour of $T = f(v_c)$ resulting from an abrupt change in machining capabilities of the cutting edge (i.e. in material constant values in formula (1)). There is no obviously known physical evidence to support such a statement. It is a sudden shift in thermomechanical behaviour of strain within the cutting zone arising from small changes in the circumstances of the process that is responsible for the externally visible transformation of chip appearance.

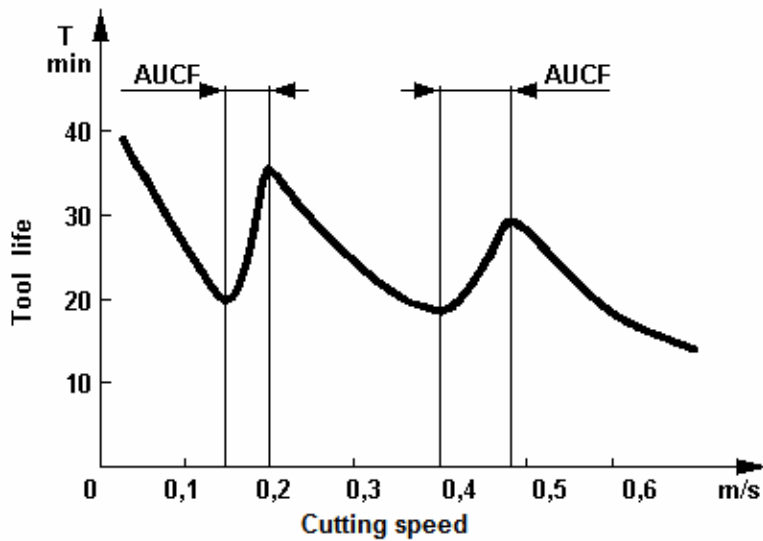


Fig. 4. Experimentally observed non-monotone behaviour of the tool-life function for Celsit SN cobalt alloy

3. Outline of theory of fuzzy sets

Fuzzy sets assigned a characteristic function which determines whether and to what extent an element possesses a certain common feature. Membership of each element in a given set is determined by that feature. A membership function varying from zero to one must be adopted. A variety of function types are available, smooth and non-smooth, the criterion of choice being simplicity, convenience, speed and efficiency or other qualities.

A fuzzy set is an extension of a classical set. If X is the universal set with elements denoted by x , then a fuzzy set A in X is defined as a set of ordered pairs (μ_A, x) , where $\mu_A(x)$ is called the membership function of x in A . The membership function maps each element of X to a membership value (degree) between 0 and 1. If the degree of membership is $\mu_A = 1$, then element x is certain to belong to set A ; if $\mu_A = 0$, then element x is surely out of the set.

If a set of elements x is a finite set of discrete values $\{x_1, x_2, \dots, x_n\}$, then the fuzzy set may be written as

$$A = (\mu_A(x_1)|x_1 + \mu_A(x_2)|x_2 + \dots + (\mu_A(x_n)|x_n). \quad (4)$$

Here the sign “+” does not stand for summation but is merely a separator between individual terms determining the degree of membership at a given point $(\mu_A(x_i)|x_i)$.

4. Application of fuzzy sets to determining the tool life

We will assume that the existence of two neighbouring chip types (denoted by A and B) within the AUCF over the cutting speed range (v_g, \dots, v_k) may be, in accordance to Figure 5, presented in the form:

a) for chip type A

$$\begin{aligned} \mu_A &= 1 && \text{for } v_c \leq v_g, \\ \mu_A &= (v_c - v_g) / (v_k - v_g) && \text{for } v_g < v_c < v_k, \\ \mu_A &= 0 && \text{for } v_c \geq v_k, \end{aligned} \quad (5)$$

b) for chip type B

$$\begin{aligned} \mu_B &= 0 && \text{for } v_c \leq v_g, \\ \mu_B &= (v_k - v_c) / (v_k - v_g) && \text{for } v_g < v_c < v_k, \\ \mu_B &= 1 && \text{for } v_c \geq v_k. \end{aligned} \quad (6)$$

The morphogenesis theory rooted in concepts developed by Thom [10, 11, 12] explains the AUCF-related phenomena as a bifurcation of function $T = f(v_c)$, i.e. the sudden appearance of an additional pattern of behaviour. Each chip type corresponds to a different pattern of strain variation, which in turn results in different values of pressures δ_N and contact temperatures Θ_s .

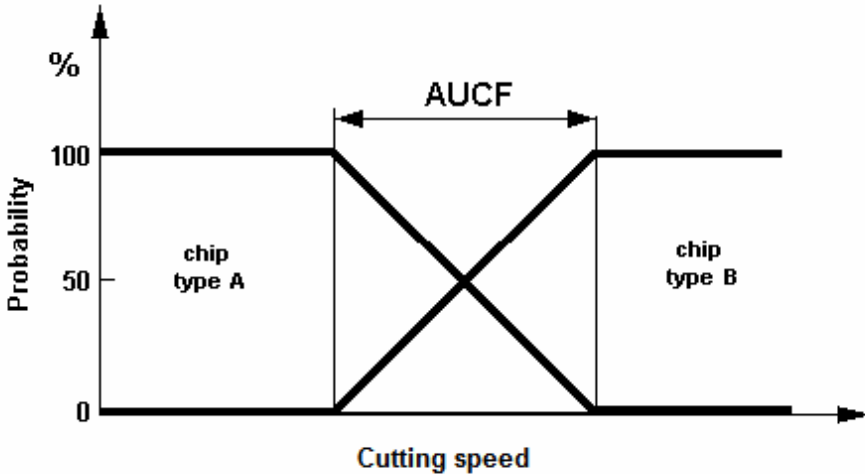


Fig. 5. Probability of occurrence of basic types of chip within AUCF

Had only the chip type A existed within the AUCF, the tool-life function for cutting speeds $v_c < v_k$ would have followed the $T_A = f(v_c)$ course. If the same is said of the B type, then the tool-life function for $v_c > v_g$ would have been in agreement with $T_B = f(v_c)$, as shown in Figure 6. However, the AUCF is composed of fuzzy sets A and B and each chip type may be assigned a degree of membership in a given set.

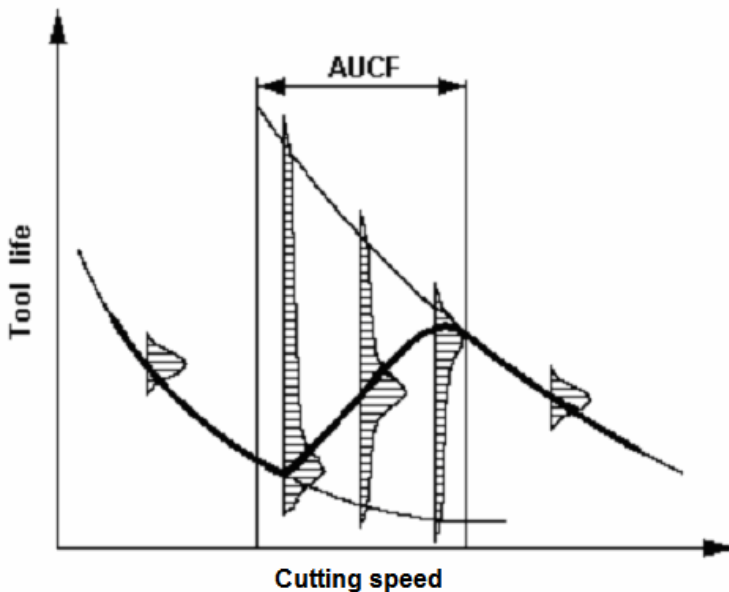


Fig. 6. Experimental scatter for a non-monotone tool-life function [7]

Both laboratory and shop-floor tests indicate that estimates of tool life are always burdened with errors arising from read-out inaccuracies and imperfections of tool geometry and tool settings. Within the ranges where the chip type remains stable, i.e. outside the cutting speed range (v_g, \dots, v_k) , scatter in the mean value of tool life may be approximated, for example, by the Gaussian distribution (Figure 6).

Statistical methods may also be used for approximating the tool life scatter within the AUCF, bearing in mind however that each chip form is characterized by its degrees of membership in particular sets. It is worth noting that tool life scatter for the AUCF cutting speeds is much broader than for cutting outside the area. This fact must be attributed to disturbed chip formation process and not to inadequate tool quality. That wide scatter within the AUCF is caused by subtle (and frequently immeasurable) changes in thermoplastic properties of workpiece material and tool geometry. As the catastrophe theory proves, even smoothly continuous processes may give rise to sharply discontinuous results, and in this case sudden variations in the thermomechanics of material deformation within the cutting zone and sharp changes in some machining indexes can occur.

A similar line of reasoning can be applied when it comes to determining variations in the mean tool-life value within the AUCF. It can be easily noted that function $T=f(v_c)$ is non-monotone with a local minimum and a maximum, both located in the vicinity of the AUCF borders. The values of $T=f(v_c)$ at any cutting speed belonging to the AUCF-related range may be found from the formula:

$$T = T_A + (\mu_A(v_c)(T_B - T_A)) = T_B - (\mu_B(v_c)(T_B - T_A)) , \quad (7)$$

where $\mu_A(v_c)$ and $\mu_B(v_c)$ are to be determined according to rules (5) and (6).

A discontinuity in the chip formation process occurring within the AUCF can be observed not only in difficult-to-machine materials but also in more easy-to-machine steels. A continuous chip transforms into a shear-localized chip within the cutting speed range of 150–1000 m/min. This range of speeds is commonly recommended for such tools as coated carbides, ceramics and cubic boron nitride (CBN).

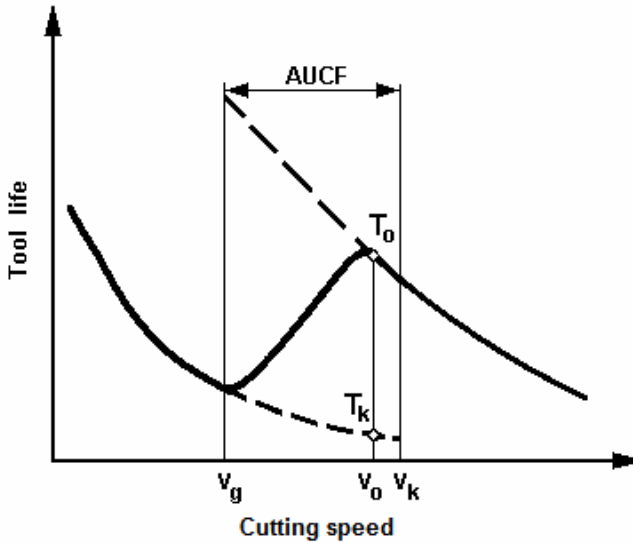


Fig. 7. Bifurcation of the $T = f(v_c)$ function within AUCF

Experimental tests serve as a basis for determining an optimum cutting speed v_{opt} ensuring the highest tool life. The life T_0 determined statistically for that speed corresponds to a local maximum of the tool-life function (Figure 7). If, however, by coincidence, thermoplastic properties of machined material and tool geometry start acting together within the AUCF to create conditions promoting a continuous chip instead of shear-localized chip, then quick dulling of a tool will occur after time T_k rather than an expected service life T_0 . This catastrophic behaviour cannot be attributed to inadequate tool quality and its real cause can be established by meticulous analysis of the chip appearance.

5. Concluding remarks

This study is an attempt to apply the theory of fuzzy sets in the explanation of non-monotone behaviour of the tool-life function and especially the occurrence of local

maxima/minima. The dynamic morphogenesis theory (catastrophe theory) is capable of modelling both continuously progressing processes (quantitative changes) and sudden jumps from one equilibrium to another (qualitative changes).

Actual machinability tests on Stellite cobalt alloys revealed the existence of the AUCF where the chip formation process undergoes a sudden change. Diffused borders separating particular chip types presented as a function of cutting parameters result from inherent inhomogeneity of machined material and elastic deformability of the tool-machine system. Non-monotonic behaviour of the tool-life function may be attributed to the disturbed mechanics of material deformation for those combinations of cutting conditions that give rise to the AUCF occurrence.

References

- [1] Taylor F.W.: *On the Art of Cutting Metals*, Amer. Mach., 1907, Vol. 28.
- [2] Podurayev V.N.: *Cutting of Difficult-to-Machine Materials* (in Russian), Vysshaya Shkola, Moscow, 1974.
- [3] Krobacher E.J., Merchant M.E.: *Basic Factors in Hot Machining of Metals*, Trans. A.S.M.E., 1951, Vol. 94.
- [4] De Almeida S.M., Hinds B.K.: *The Influence of Temperature on the Machinability of Stellite 6*, Proc. 21-th Int. Mech. Tool Des. Res. Conf., Swansea, 1980.
- [5] Miernik M.: *Bases of Cutting Cobalt Alloys* (in Polish), Scientific Papers of the Institute of Machine Building Technology No. 41, Monographs No. 9, Wrocław University of Technology, 1989.
- [6] Miernik M.: *The Tool Life in the Regions of Undetermined Cutting* (in Polish), Scientific Papers of the Institute of Machine Building Technology No. 31, Conferences No. 9, Wrocław University of Technology, 1986.
- [7] Miernik M.: *Application of the Catastrophe Theory to the Study on the Chip Formation Process*, Eur. J. Mech. Ing., 1992, Vol. 37, 1.
- [8] De Almeida S.M., Miernik M., Żebrowski H.: *Influence of Microstructure on Chip Formation and Machinability of Some Cobalt Alloys*, Material Science and Technology, 1988, Vol. 4.
- [9] Cieślak M., Smoluk A.: *Fuzzy sets. Image Recognition. Catastrophe Theory* (in Polish), PWN, Warszawa, 1988.
- [10] Thom R.: *Mathematical Models of Morphogenesis*, J. Wiley and Sons Inc., New York, 1983.
- [11] Poston T., Steward I.: *Catastrophe Theory and its Applications*, Pitman Publ. Ltd., London, 1981.
- [12] Klamecki B.E.: *Catastrophe Theory Model of Chip Formation*, Trans. A.S.M.E., J. Eng. for Ind., 1982, Vol. 104, 4.
- [13] Von Turkovich B.F.: *Influence of Very High Cutting Speed on Chip Formation Mechanics*, Proc. N.A.M.R.C., 1979, Vol. 7.
- [14] Komanduri R. et al.: *On the Catastrophic Shear Instability in High-Speed Machining of an AISI 4340 Steel*, Trans. A.S.M.E., J. Eng. for Ind., 1982, Vol. 104, 2.

Zastosowanie teorii zbiorów rozmytych do analizy niemonotoniczności okresu trwałości ostrza

Przedstawiono przykłady niemonotoniczności funkcji okresu trwałości ostrza podanej przez Taylora. Wykazano doświadczalnie powiązanie między występowaniem podstawowych odmian wióra (wiór segmentowy, wiór ciągły, wiór piłozębny o zlokalizowanych strefach ścinania) a niemonotonicznością funkcji okresu trwałości ostrza skrawającego na przykładzie ortogonalnego toczenia poprzecznego stopów kobaltowych typu stellit. Zaprezentowano próbę wyjaśnienia przyczyn powstawania niemonotoniczności funkcji okresu trwałości funkcji, opierając się na teorii zbiorów rozmytych. Podano reguły obowiązujące w tzw. „obszarach nieokreślonego przebiegu formowania wióra”, a dotyczące lokalnych minimów i maksimów funkcji Taylora. Przedstawiono krótki zarys teorii zbiorów rozmytych w ujęciu bifurkacji przebiegu okresu trwałości ostrza, w ujęciu dynamicznej teorii morfologii R. F. Thoma (tzw. teorii katastrof).

Analysis of surface roughness profile after its machining in terms of nonlinear dynamics

M. MIERNIK, J. SZYMKOWSKI, M. WIĄCEK

Wrocław University of Technology, Wybrzeże Wyspiańskiego 25, 50-370 Wrocław

The feed influence on nonlinear changes of the surface roughness after its machining was presented. It was revealed that the derivative of the roughness factor was discontinuous in the function of feed. The roughness profile of a real surface depended on some random factors. Application of fractals (in the form of chaotic attractors) to the analysis of the surface roughness profile after turning was presented. The effect of feed rate and cutting speed on the fractal dimension and the maximum value of Lapunov exponent as well as on the representation characteristics of cutting process in 3D phase surface were evaluated.

Keywords: *surface roughness, machining, nonlinear dynamics*

1. Introduction

Most goods produced by man are made by machining. This method involves the greatest costs, which encourages us to make a right and wise choice of conditions for such a process. The machining process is named dimensional and surface creating. Construction of a comprehensive machining model that describes genesis of outer layer constitution and allows its comparison to real results is essential.

2. Theoretical model of surface roughness

The first attempt to develop a mathematical model of cutting process was undertaken at the beginning of the twentieth century by Taylor [1] who arrived at statistic-experimental equation for wedge substance. Another model, elaborated by Kaczmarek [2], is based solely on geometric-kinematic mapping (Figure 1).

Making an assumption that nose radius r and the tool cutting edge angles κ and κ_1 (κ is main angle and κ_1 is minor one) are constant, we can claim that particular cases of mapping depend on feed rate only, and the values of feed, which are considered to be the limits between mapping cases, are called the limit feeds.

The first case of mapping takes place when transverse traces of mapping are formed due to crossing the arch parts of the cutting edge (Figure 1a) – this is arch mapping. This case occurs when:

$$\begin{aligned} f \leq f_1 &= 2 \cdot r \cdot \sin \kappa_1, & \text{if } \kappa > \kappa_1, \\ f \leq f_1 &= 2 \cdot r \cdot \sin \kappa, & \text{if } \kappa < \kappa_1. \end{aligned} \quad (1)$$

The second case of mapping (Figure 1b) occurs when transverse traces of mapping appear as a result of crossing the arch and straight-line parts of cutting edge and is called the arch–straight-line mapping.

This case takes place for

$$2 \cdot r \cdot \sin \kappa_1 < f < 2 \cdot r \cdot \frac{\sin^2\left(\frac{\kappa + \kappa_1}{2}\right)}{\sin \kappa_1}, \quad \text{if } \kappa > \kappa_1, \quad (2)$$

$$2 \cdot r \cdot \sin \kappa < f < 2 \cdot r \cdot \frac{\sin^2\left(\frac{\kappa + \kappa_1}{2}\right)}{\sin \kappa}, \quad \text{if } \kappa < \kappa_1.$$

In the third case (Figure 1c), the transverse traces of mapping appear as a result of crossing straight-line parts of cutting edge. This is the straight-line mapping case which takes place for:

$$f \geq 2 \cdot r \cdot \frac{\sin^2\left(\frac{\kappa + \kappa_1}{2}\right)}{\sin \kappa_1}, \quad \text{if } \kappa > \kappa_1, \quad (3)$$

$$f \geq 2 \cdot r \cdot \frac{\sin^2\left(\frac{\kappa + \kappa_1}{2}\right)}{\sin \kappa}, \quad \text{if } \kappa < \kappa_1.$$

Based on the theoretical model of the roughness described above it was possible to plot the curve representing the theoretical roughness R_{zt} (Figure 2).

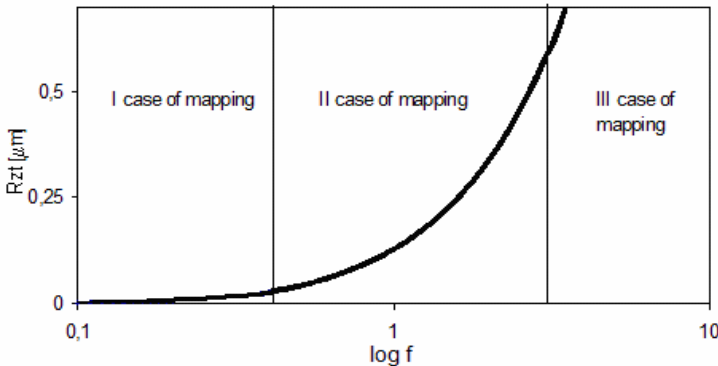


Fig. 2. Theoretical roughness R_{zt} versus $\log f$ for I, II and III cases of mapping

Theoretical surface roughness R_{zt} and feed limits are listed in the Table.

Table. Theoretical surface roughness

| | | | | |
|-------------------------|----------|---|--|---|
| For $\kappa > \kappa_1$ | R_{zt} | $r - 0.5\sqrt{4r^2 - f^2}$ | $f \left(\frac{\sin 2\kappa_1}{2} - \sin \kappa_1 \cdot \sqrt{\frac{2r}{f \sin \kappa_1} - 1} \right) + 2 \cdot r \cdot \sin^2 \left(\frac{\kappa_1}{2} \right)$ | $f \frac{\sin \kappa \sin \kappa_1}{\sin(\kappa + \kappa_1)} - 1 \times \left[\frac{\sin \kappa + \sin \kappa_1}{\sin(\kappa + \kappa_1)} - 1 \right]$ |
| | Feed | $f \leq f_1 = 2r \sin \kappa_1$ | $f_1 < f < f_2$ | $f \geq f_2 = 2r \frac{\sin^2 \left(\frac{\kappa + \kappa_1}{2} \right)}{\sin \kappa_1}$ |
| | Symbol |  |  |  |
| Case of mapping | I | II | III | |
| | Symbol |  |  |  |
| For $\kappa < \kappa_1$ | Feed | $f < f_1 = 2r \sin \kappa$ | $f_1 < f < f_2$ | $f \geq f_2 = 2r \frac{\sin^2 \left(\frac{\kappa + \kappa_1}{2} \right)}{\sin \kappa}$ |
| | R_{zt} | $r - 0.5\sqrt{4r^2 - f^2}$ | $f \left(\frac{\sin 2\kappa}{2} - \sin \kappa \cdot \sqrt{\frac{2r}{f \cdot \sin \kappa} - 1} \right) + 2 \cdot r \cdot \sin^2 \left(\frac{\kappa}{2} \right)$ | $f \frac{\sin \kappa - \sin \kappa_1}{\sin(\kappa + \kappa_1)} - 1 \times \left[\frac{\sin \kappa + \sin \kappa_1}{\sin(\kappa + \kappa_1)} - 1 \right]$ |

The curve in Figure 3 represents geometric-kinematic dependences only. Thus, physical and chemical phenomena in workpiece cutting such as: machine tool properties, edge design, lubricant influence and tool wear are not taken into account.

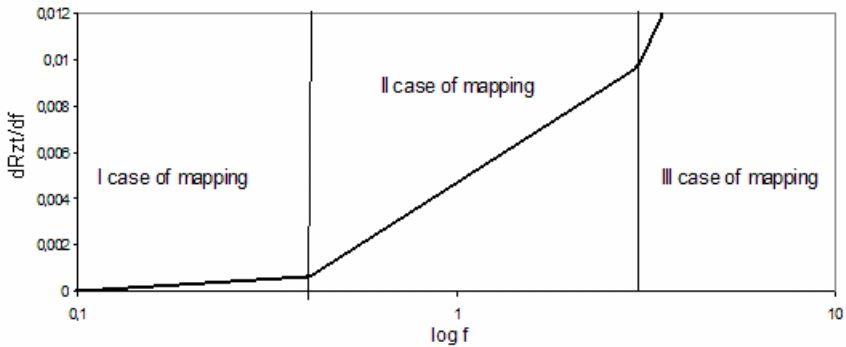


Fig. 3. Roughness function versus feed

Besides those factors a real roughness is influenced by chip trajectory, mechanical vibration, cutting temperature and cutting force components. Furthermore it was proven that derivative of the theoretical roughness function versus feed was discontinuous. Based on this statement we can conclude that real profile of roughness depends on many random factors and that in the limit feed zone it is difficult to define these phenomena.

In reality, theoretical roughness differs substantially from real one (Figure 4).

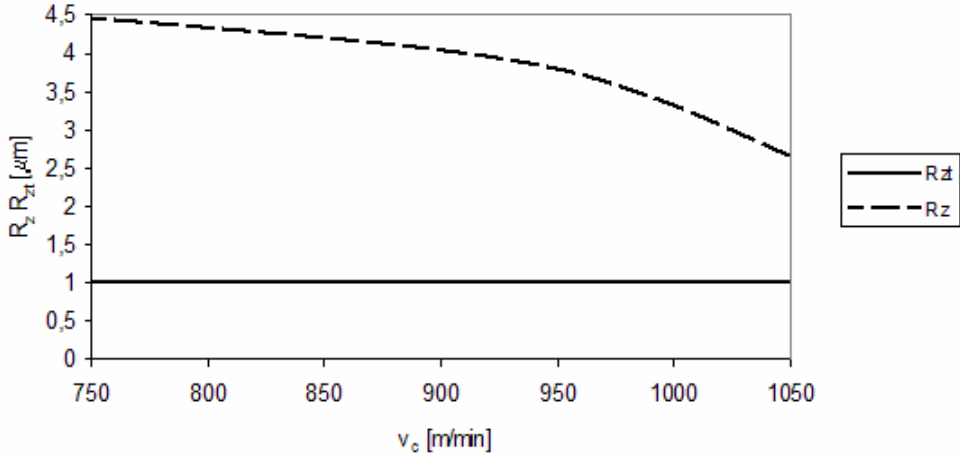


Fig. 4. Theoretical and real roughnesses versus cutting speed

3. Surface roughness in nonlinear dynamics

Theoretical models described above are imperfect. They have to be supplemented with many factors accompanying the cutting process. It is very difficult to design a mathematical model on the basis of theory only, therefore such a model does not exist so far. It is obviously more probable that this model will be constructed on the basis of cutting process observation [3]. To that end the cutting parameters have to be chosen automatically and exact analytical solution will not be necessary, because the cutting process is accompanying by random disturbances.

Due to the above reasons, since over ten years the analysis of nonlinear dynamics cutting process based on unconventional mathematical methods has been highly advanced. These methods are as follows:

- theory of dynamic morphogenesis,
- elements of fuzzy logic,
- artificial neural networks and genetic algorithm,
- fractal techniques connected with chaos theory.

The methods of construction of cutting models that concern linear and nonlinear dynamics are presented in Figure 5.

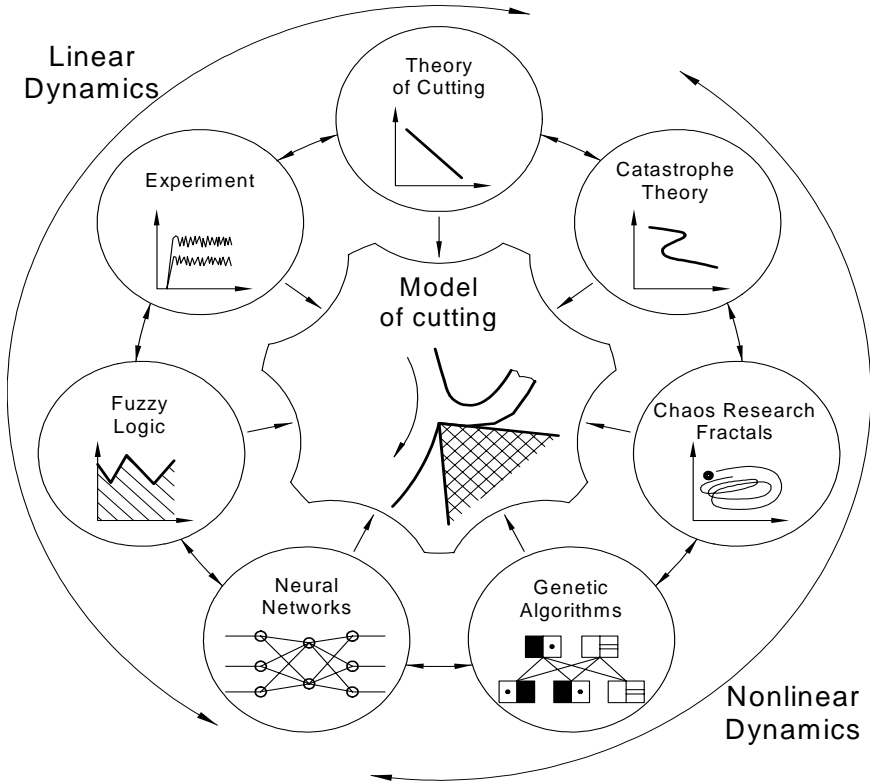


Fig. 5. The methods of modeling the cutting process [5]

Up to now fractal analysis in connection with Lapunov's exponent (λ) monitoring has been the most often used techniques. The exponent (λ) represents a number of valuable information about both the nature of a cutting process and surface subjected to cutting and can be calculated from the expression:

$$\lambda_i = \lim_{t \rightarrow \infty} \lim_{\varepsilon \rightarrow 0} \frac{\varepsilon_i(t)}{t\varepsilon_i(0)}; \quad i=1, \dots, d_1, \quad (4)$$

where:

λ_i – calculated exponent for phase space of the i -th direction,

d_1 – local dimension of attractor,

t – time,

$\varepsilon_i(0)$ – location of an initial trajectory,

$\varepsilon_i(t)$ – trajectory location after time t .

The analysis of Lapunov's exponent consists in choosing its biggest value and determining its plus/minus sign. Positive sign ($\lambda > 0$) denotes the condition at which

a chaotic system exists. The fractal analysis allows creating the so-called chaotic attractors and determining fractal dimension. Characteristics of these both factors change together with the cutting parameters.

In Figure 6, the attractors for regular elements are presented. They have no connection with nonlinear dynamics, but are shown for the purpose of cognition.

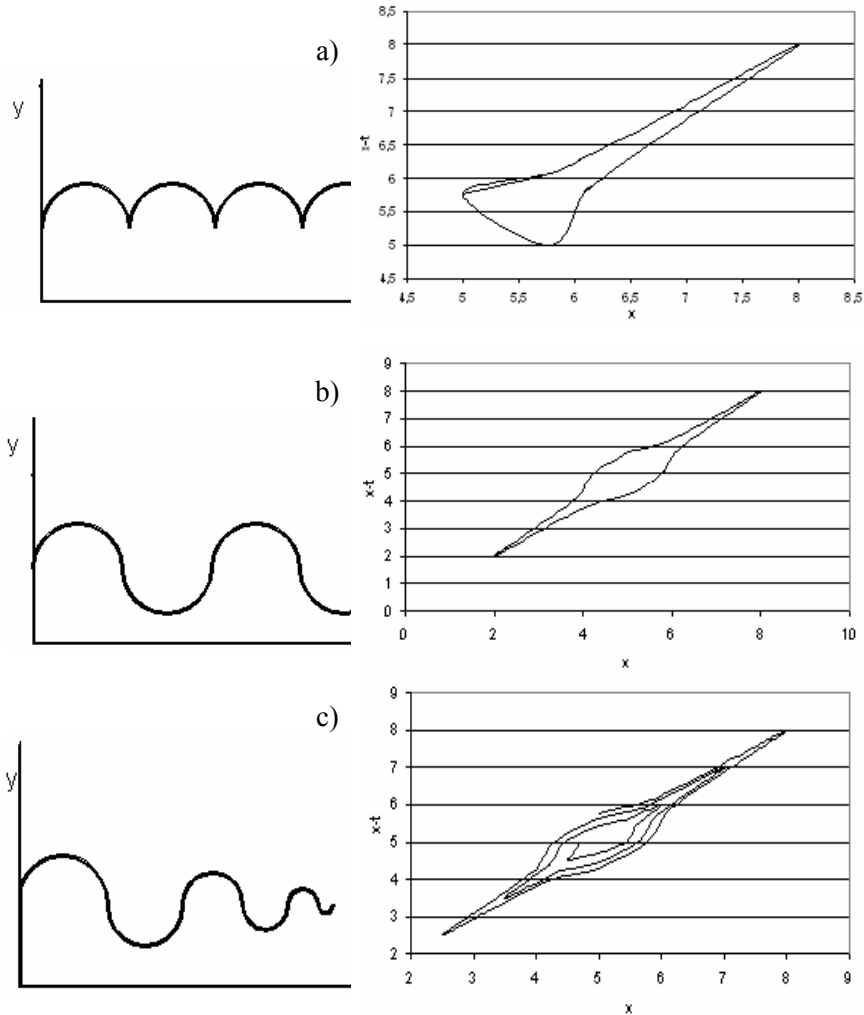


Fig. 6. Geometrically regular objects and their attractors

4. Experiment conditions

The purpose of the experiments was to collect an indispensable data in the form of surfaces of alloy cast-iron workpiece machined by turning in a wide range of cutting parameters. Cutting tool CSRNR 2525-12 with $\kappa = 75^\circ$ and $\kappa_1 = 15^\circ$ was used. Inserts SNGN 120408T0202 with PVD coatings and the nose radius $r = 0.8$ mm were used. Cutting speed was varied in the range of 750–1050 m/min, feed of 0.08–0.24 mm/rev, and depth of 0.5–1 mm. Roughness parameters were measured using Form Talysurf 120L Taylor Hobson device.

5. Results of investigations

In all cases, the calculated values of the greatest Lapunov's exponent were bigger than zero which suggested that the surfaces investigated had a chaotic character.

Chaotic attractors created on the basis of phase delay [4] are presented as irregular loops (one loop corresponds to the feed value defined) in Figure 7b.

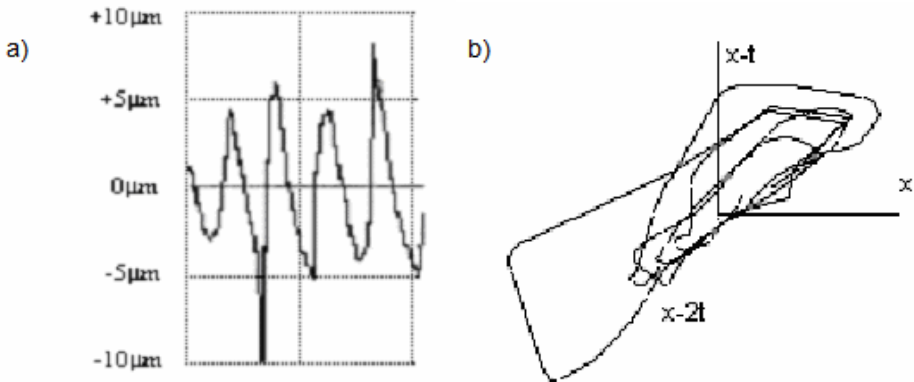


Fig. 7. Profile of alloy cast-iron being turned ($v_c = 900$ m/min, $f = 0.24$ mm/rev, $a_p = 1$ mm) (a), its chaotic attractor (b)

It has been also revealed that fractal dimension decreases together with a decrease in the values of roughness parameters, i.e. indirectly with an increase in cutting speed and a decrease in feed.

6. Conclusions

1. Fractal dimension can be helpful as an additional parameter characterizing the surface being machined.

2. A decrease in feed is accompanied with an increase in fractal dimension. The concentration of non-ordered loops on geometrical mapping can be seen which was proven by the experiment [6].

3. Fractal analysis could be helpful in the analysis of surface roughness.
4. Both fuzzy logic elements and neural networks can be fruitful in creating monitoring systems for machining in real time (on-line).

References

- [1] Taylor F.W.: *On the Art of Cutting Metals*. Amer. Mach., 1907, Vol. 28.
- [2] Kaczmarek J.: *Podstawy obróbki wiórowej, ściernej i erozyjnej*, Wydawnictwo Naukowo-Techniczne, Warszawa, 1970.
- [3] Jemielniak K.: *Obróbka skrawaniem*, Oficyna Wydawnicza Politechniki Warszawskiej, Warszawa, 1998.
- [4] Ott E.: *Chaos w układach dynamicznych*, Wydawnictwa Naukowo-Techniczne, Warszawa, 1997.
- [5] Miernik M.: *Skrawalność metali. Metody określania i prognozowania*, Oficyna Wydawnicza Politechniki Wrocławskiej, Wrocław, 2000.
- [6] Broll S., Grzesik W.: *Zastosowanie analizy fraktalnej do oceny profilu chropowatości powierzchni. Zagadnienia inżynierii powierzchni w obróbce skrawaniem*, Międzynarodowe Sympozjum Inżynieria Powierzchni '99, Wrocław–Szklarska Poręba, 7–9.06.1999.

Analiza profilu chropowatości powierzchni po obróbce skrawaniem w ujęciu dynamiki nieliniowej

Przedstawiono analizę wpływu posuwu skrawania na nieliniowość zmian chropowatości powierzchni. Wykazano, że pochodna wskaźnika chropowatości jest nieciągła w funkcji posuwu, a profil chropowatości powierzchni rzeczywistej zależy od czynników losowych. Przedstawiono wyniki badań nad zastosowaniem fraktali (chaotycznych atraktorów) do analizy profilu chropowatości powierzchni po toczeniu. Oceniono wpływ posuwu i prędkości skrawania na wymiar fraktalny i największy wykładnik Lapunowa oraz na charakter odwzorowania dynamiki procesu skrawania w trójwymiarowej przestrzeni fazowej.

Correction of geometrical defects of stamping parts by numerical simulation and design of experiment

E. PAIREL, Y. LEDOUX, R. ARRIEUX, L. TABOUROT, O. INCANDELA

Laboratory of Applied Mechanics, University of Savoy, BP 806, 74016 ANNECY Cedex, France

A method of correction and optimization of stamping processes is proposed. The experiment design and finite element methods are interfaced. This is applied in a part showing large springback. After determining some important process parameters that affect springback, a fractional factorial experiment design is built and the corresponding numerical simulations are carried out. This enabled us to obtain deformed meshes which were post-processed in order to measure a virtual part geometry. Linear mathematical relations between the part geometry and process parameters are established which allows determining their interactions and their influence on the geometrical shape of parts. Finally those mathematical relations were necessary for establishing correct values of the process parameters which lead to the expected geometry of parts.

Keywords: *stamping, design of experiments, finite element method, elastic springback, tool optimization*

1. Introduction

With an increasing complexity of product geometry, it is more and more difficult to determine the tool geometry and the process parameters of a deep drawing operation. Furthermore, the designers want to control the geometry of the final product with a precision that requires the compensation for the tool geometry in order to take into account elastic deflections that occur after the operation. Empirical rules combined with costing trial and error method are used to find a right combination of process parameters.

Finite element technique may be used to assist engineers but it often poorly reflects the reality because of an approximate modelling both the process and the material behaviour. Even in this case, the optimization method is still a trial and error method.

In fact, whatever the technique used to optimize the deep-drawing operation, one is often unable to deal with complex interaction between the factors influencing this operation. Optimization of complex parts is then a hazardous procedure that often leads to delay, the lack of quality and costing adjustment of the tool geometry (when it is still possible!) and the process parameters.

Nevertheless the design and optimization of the drawing process must be considered using the finite elements simulation.

This paper proposes an alternative to this (lack of) technique. It shows the interest in the application of the design of experiments to deep-drawing process during the process optimization phase in combination with the finite element simulations. In or-

der to illustrate the application of the method proposed, a simple piece providing large elastic deflection is adopted.

In the section 2, previously related works are analysed. Section 3 presents the proposed method and discusses its results. Finally a conclusion will be presented in section 4.

2. Existing methods

Two approaches can be found in the literature:

The first one, consists in virtually “deforming” the tool in the opposite direction compared to the observed springback on the computed part. Such an approach presented Zimniak in [1]. It makes it possible to obtain, in some iterations, the shape of the tool which enables us to “compensate” the springback of the part. It does not allow the optimization of such process conditions as blankholder force or punch velocity, which are of great importance.

Another approach suggested by Browne and Hillery [2] consists in carrying out real tests by using the Design of Experiments (DOE) method and searching for the best combination of the manufacturing parameters from these tests. Colgan and Monaghan [3] designed a similar experiment to determine the parameters that affect the thickness distribution on the part being formed.

3. The method proposed

The suggested method consists in identifying the relations between the geometry of the part being formed and some manufacturing parameters due to a succession of simulations defined by an experiment design. Then, those relations allow the determination of one or more sets of values for the manufacturing parameters, leading to the expected shape of a part.

The method has seven stages presented here on a stamped part chosen for its simplicity and its important springback. It is a V-shaped aluminium part. Figure 1 shows its definition drawing and its dimensions.

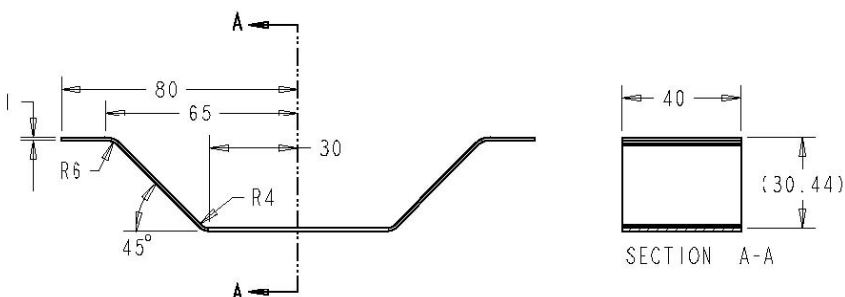


Fig. 1. Definition drawing of the part

The stamping process is presented in Figure 2 in the “formed part” position. The shape of the part in the tool corresponds to the expected shape and does not take the springback into account.

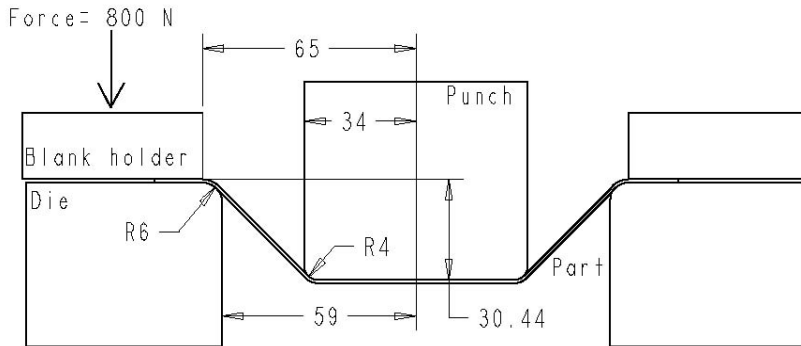


Fig. 2. Initial stamping process in the final position

3.1. Stage 1: simulation of the initial designed stamping process

The first simulation is carried out with the simple tooling shown in Figure 2 in order to check the elastic deflections. The finite-element calculation software Explicit ABAQUS is used. The material used is an 6061 T4 aluminium alloy sheet. The behaviour law is determined based on tensile tests using an extensometer and an image analysis system for the high-strain levels [4]. It is introduced point by point in the calculation software. An elastoplastic isotropic behaviour is assumed. Four layers of 2D rectangular elements allow a part modelling. The element size is smaller in the part areas which will be strongly strained. The contact between the tools and the blank is of the Coulomb type with a friction coefficient $f = 0.1$ determined by experience.

Taking an isotropic character of aluminium into account, it is decided to realise a planar simulation on half of the profile only (see Figure 3). The simulation of the initial stamping process gives the shape of the part presented in Figure 3.



Fig. 3. Shape of the part obtained by simulation with the initial process

It can be observed that the straight segments of the part keep their rectilinear shape. The defects are essentially dimensional defects: the angle between the bottom and the

lateral edge is upper than 135° , so an elastic deflection opens the angle after a simple bending operation, as expected; while the angle between the lateral edge and the upper flange is lower than 135° , this means that an elastic deflection closes the angle after a bending–unbending operation on the die radius.

The angles do not have the right values and consequently the height is not enough. So it is decided to characterise those defects by linear and angular parameters (stage 2).

3.2. Stage 2: parametrization of the geometrical defects of the part

Taking into account the observed geometrical defects of the part, it is now necessary to characterize them by dimensional parameters which will be measurable on the simulated strained part.

We assume that the profile is composed of straight segments and arcs of circle or of ellipse. These theoretical features will be fitted on the profile of the virtual part, constituting of a set of nodes, in stage 5. This fitting enables us to define the size and location parameters.

It is necessary to redraw the part with the location defects between geometrical features in order to reveal the implicit parameters of the definition drawing (A2 in this example).

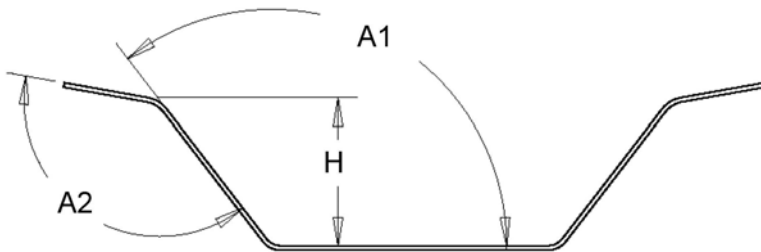


Fig. 4. Parameter setting of the part having location defects

Several parameter settings of the geometry are possible. For the part studied, three important geometrical parameters revealing elastic deflections are selected: the two angles $A1$, $A2$ and the distance H shown in Figure 4. The radii are not taken into account.

Those parameters will be measured on the simulated part at stage 5.

3.3. Stage 3: searching for the parameters that affect the stamping process

As the previous stage, this one needs also thinking about. It consists in searching for the process parameters that will be able to affect the selected geometry parameters of the part. Moreover, they must be strictly independent of each other: this means that the variation of one of them must be obtained without modification of the others.

The selected process parameters are shown in Figure 5. They are as follows: die angle A , die radius R , die width W , punch travel D and blankholder force F .

Those parameters and their variation range are chosen according to the initial simulation and to the observations of their probable influence. Their values are given in Table 1.

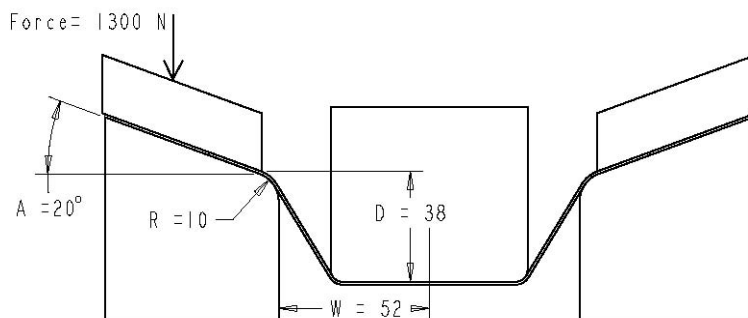


Fig. 5. Tool parameters

Table 1. Tested parameters of the stamping process with their fields of variation

| Parameter | Initial value | Low value (-1) | High value (+1) |
|--------------------------------|---------------|----------------|-----------------|
| A : angle of the die | 0° | 0° | 20° |
| R : radius of the die | 6 mm | 6 mm | 10 mm |
| W : width of the die | 59 mm | 52 mm | 59 mm |
| D : depth of the punch | 30.44 mm | 33 mm | 38 mm |
| F : force of the blankholder | 800 N | 5 N | 1000 N |

Finally three equations will be obtained, each representing one geometrical parameter, i.e. A_1 , A_2 and H , as a function of the five process parameters, A , R , W , D , and F .

3.4. Stage 4: choice of the model and construction of the experiment design

Here we select the first-degree polynomial model which assumes a linear variation of the output from every input:

$$Y = a_0 + a_1A' + a_2R' + \dots + a_5F' + a_{12}A'R' + \dots + a_{45}D'F' \text{ (where } Y \text{ is } A_1, A_2 \text{ or } H).$$

In this model, the terms X_i, X_j are the interactions between factors, this means that the effect of one of them X_i depends on the value of the other one X_j .

We use a fractional experiment design in order to decrease a number of numerical simulations. For five factors it is necessary to carry out sixteen numerical experiments as shown in Table 2, while for a full factorial experiment design, 32 experiments should be necessary. For every variable, two levels are tested: a low and a high ones defined in Table 1. In Table 2, the levels -1 and $+1$ correspond respectively to a low value and a high value of the parameter.

Table 2. Experiment design with two levels to test the stamping parameters (a low value of the factor is noted “ -1 ” and a high value “ $+1$ ”)

| No. of the experiment | Angle of the die A | Radius of the die R | Width of the die W | Depth of the punch D | Force of the blank-holder F | Result |
|-----------------------|----------------------|-----------------------|----------------------|------------------------|-------------------------------|---------------------|
| 1 | -1 | -1 | -1 | -1 | -1 | Simulated profile 1 |
| 2 | -1 | -1 | -1 | $+1$ | $+1$ | Simulated profile 2 |
| 3 | -1 | -1 | $+1$ | -1 | $+1$ | Simulated profile 3 |
| 4 | -1 | -1 | $+1$ | $+1$ | -1 | Simulated profile 4 |
| 5 | -1 | $+1$ | -1 | -1 | $+1$ | Simulated profile 5 |
| 6 | -1 | $+1$ | -1 | $+1$ | -1 | Simulated profile 6 |
| 7 | -1 | $+1$ | $+1$ | -1 | -1 | Simulated profile 7 |
| 8 | -1 | $+1$ | $+1$ | $+1$ | $+1$ | Simulated profile 8 |

Table 2. Experiment design with two levels to test the stamping parameters (a low value of the factor is noted “ -1 ” and a high value “ $+1$ ”)

| No. of the experiment | Angle of the die A | Radius of the die R | Width of the die W | Depth of the punch D | Force of the blank-holder F | Result |
|-----------------------|----------------------|-----------------------|----------------------|------------------------|-------------------------------|----------------------|
| 9 | $+1$ | -1 | -1 | -1 | $+1$ | Simulated profile 9 |
| 10 | $+1$ | -1 | -1 | $+1$ | -1 | Simulated profile 10 |
| 11 | $+1$ | -1 | $+1$ | -1 | -1 | Simulated profile 11 |
| 12 | $+1$ | -1 | $+1$ | $+1$ | $+1$ | Simulated profile 12 |
| 13 | $+1$ | $+1$ | -1 | -1 | -1 | Simulated profile 13 |
| 14 | $+1$ | $+1$ | -1 | $+1$ | $+1$ | Simulated profile 14 |
| 15 | $+1$ | $+1$ | $+1$ | -1 | $+1$ | Simulated profile 15 |
| 16 | $+1$ | $+1$ | $+1$ | $+1$ | -1 | Simulated profile 16 |

3.5. Stage 5: measurement of the dimensional parameters on the simulated parts

Each experiment corresponds to a numerical simulation carried out with the equivalent process parameters. The result is a file of points which are the nodes of the mesh of the simulated part being formed after the tools removing. This file is post-treated in order to measure the geometrical parameters. The results are shown in Table 3.

The measurement principle consists in conducting the following geometrical operations:

1. First, it is necessary to extract the upper layer of the cloud of points issued from the simulation and to divide it into the areas corresponding to the geometrical feature of the part. For a profile, these features are mainly straight segments and arcs of circle.

2. Second, a perfect geometrical feature is fitted to each area of points, according to the least square criterion. If it is an arc of circle, its radius is measured.

3. Third, the distances and the angles between the geometrical features are measured (angle between two lines or distance between a line and a point).

Table 3. Measurement results on the sixteen simulated parts

| No. of the experiment | Angle A1 (°) | Angle A2 (°) | High <i>H</i> (mm) |
|-----------------------|--------------|--------------|--------------------|
| 1 | 132.89 | 116.89 | 27.79 |
| 2 | 120.02 | 116.55 | 37.51 |
| 3 | 132.03 | 131.23 | 32.97 |
| 4 | 135.76 | 121.09 | 31.72 |
| 5 | 126.56 | 124.82 | 32.63 |
| 6 | 132.89 | 115.86 | 30.85 |
| 7 | 145.06 | 132.63 | 24.98 |
| 8 | 131.52 | 131.8 | 36.20 |
| 9 | 123.25 | 140.92 | 32.52 |
| 10 | 125.26 | 130.24 | 32.53 |
| 11 | 143.92 | 150.05 | 23.02 |
| 12 | 128.12 | 147.25 | 36.95 |
| 13 | 137.44 | 138.64 | 23.99 |
| 14 | 120.26 | 138.97 | 37.78 |
| 15 | 133.01 | 152.64 | 33.16 |
| 16 | 142.41 | 149 | 25.76 |

3.6. Stage 6: calculation and validation the polynomial models $Y=f(X)$

From the results of the experiment design the coefficients of the polynomial model of every output $A1$, $A2$ and H are calculated:

The general method for calculating these coefficients is a multilinear regression. With the sixteen experiments of the fractional experiment design, the following equations are obtained (the most significant effects are in bold type):

$$A1 = \mathbf{131.90} - 0.19A' + \mathbf{1.74R'} + \mathbf{4.58W'} - \mathbf{2.37D'} - \mathbf{5.05F'} - 0.17A'R' + 0.58A'W' - 0.32A'D' - 0.5A'F' - 0.22R'W' + 0.49R'D' - 0.75R'F' + 0.35W'D' - 0.26W'F' + 0.51D'F',$$

$$A2 = \mathbf{133.66} + \mathbf{9.80A'} + \mathbf{1.88R'} + \mathbf{5.8W'} - \mathbf{2.32D'} + \mathbf{1.86F'} - 0.53A'R' + 0.47A'W' + 0.22A'D' - 0.38A'F' + 0.17RW - 0.68RD - 0.35RF + 0.14WD - 0.59WF + 0.43DF,$$

$$H = \mathbf{31.27} - 0.56A' - 0.60R' - 0.68W' + \mathbf{2.39D'} + \mathbf{3.69F'} + 0.06A'R' - 0.31A'W' + \mathbf{0.15A'D'} + 0.70A'F' + 0.03R'W' - 0.41R'D' + 0.58R'F' - 0.33W'D' + 0.53W'F' - 0.25D'F'.$$

A' , R' , W' , D' and F' are the standardised variables, respectively corresponding to the die angle A , the die radius R , the die width D , the punch travel W and the tightening force F . They vary from -1 to $+1$ when the corresponding variable varies from a low value to a high one.

Each of the three models must be validated. For that, three verifications are made:

1. First, the ability of the model to predict the value of the output for any extreme configuration of the factors, i.e. a configuration such that the factors have the value -1 or the value $+1$, is checked. These configurations are called the nodes of the study field. There are thirty two $(2)^5$ nodes. Sixteen were already measured in the experiment design. For five factors, the adopted models have sixteen independent coefficients, which enables them to pass exactly by the sixteen experimental points of the experiment design. So, this first verification is useless here.

It is thus necessary to test these models on nodes out of the experiment design. One can choose a configuration which, according to the model, gives the minimal or maximum value to the output. In this example, exceptional fact, the configuration given in Table 4 gives, according to the polynomial models, simultaneously the maximum value with the $A1$ and $A2$ angles and the minimum value for the height H .

One notes that the values predicted by the models deviate from the actual values. The models thus do not seem very precise when the manufacturing parameters have extreme values not tested in the experiment design.

As it is not into the plan, it enables us to test the three models:

Table 4: Verification of the models on a particular configuration out of the experiment design

| No. | A' | R' | W' | D' | F' | $A1$ | $A2$ | H |
|-----|------|------|------|------|------|--------------------|-------------------|--------------------|
| 17 | 1 | 1 | 1 | -1 | -1 | Theoretica: 147.1° | Theoretic: 152.4° | Theoretic: 21.7 mm |
| | | | | | | Realb: 142.8° | Real: 149.9° | Real: 25.4 mm |
| | | | | | | Deviationc: 4.3° | Deviation: 2.5° | Deviation: -3.7 mm |

a – obtained with the polynomial model.

b – obtained with the numerical simulation by FEM.

c – (Y theoretic – Y real).

2. The third verification, consist in checking the ability of the model to predict the value of the output inside the field of study, i.e. when the factors have intermediate values between -1 and $+1$. For that, the model is tested at the center of the field of study, i.e. when the standard variables are equal to zero and the real variables are equal to their average values.

Table 5: Verification of the models at the center of the field of study

| No. | A' | R' | W' | D' | F' | $A1$ | $A2$ | H |
|-----|------|------|------|------|------|--------------------|-------------------|--------------------|
| 18 | 0 | 0 | 0 | 0 | 0 | Theoretica: 131.9° | Theoretic: 133.7° | Theoretic: 31.3 mm |
| | | | | | | Realb: 130.2° | Real: 132.4° | Real: 33.2 mm |
| | | | | | | Deviationc: 1.7° | Deviation: 1.3° | Deviation: -1.9 mm |

a – obtained with the polynomial model.

b – obtained with the numerical simulation by FEM.

c – (Y theoretic – Y real).

One notes again that the models deviate from reality, but the differences are lower than in the preceding extreme configuration.

To improve the precision of the models, it would be necessary to increase the number of tests of the experiment design to enable one to calculate the interactions of the order of 3 and higher and to introduce quadratic terms in order to model the non-linearity of the phenomena.

In the continuation, the search for the optimal solutions is undertaken with these models by privileging the solutions close to the experimental points of the experiment design in order to limit the error of prediction of the models.

3.7. Stage 7: search for optimal values of stamping process parameters

The objective is to determine the values of the process parameters which allow one to obtain the best values of the part parameters, i.e. as close as possible to the target values: $A1 = 135^\circ$, $A2 = 135^\circ$ and $H = 30.44$ mm. The principle consists in minimiz-

ing a function equal to the sum of the deviations between the theoretical and the desired output. In order to keep this sum positive, the deviations are squared:

$$F = (A1 - 135^\circ)^2 + (A2 - 135^\circ)^2 + (H - 30.44)^2.$$

This function has several local minima in the field of study defined by the values -1 and $+1$ of the process parameters. Most of them are shown in Table 6, sorted on the angle A :

Table 6. Several optimal solutions

| No. of optimal solution | Angle of the die $A' A$ | Radius of the die $R' R$ | Width of the die $W' W$ | Depth of the punch $D' D$ | Blankholder force $F' F$ |
|-------------------------|-------------------------|--------------------------|-------------------------|---------------------------|--------------------------|
| 1 | 0.35 13.5° | -1 6 mm | 0.75 58.1 mm | 1 38 mm | -0.91 47 N |
| 2 | 0.28 12.8° | -1 6 mm | 0.74 58.1 mm | 0.82 37.5 mm | -0.8 104.5 mm |
| 3 | -0.04 9.5° | 0.82 9.6 mm | 0.24 56.3 mm | 0.45 36.6 mm | -0.26 372 N |
| 4 | -0.16 8.3° | 0.03 8.0 mm | 0.50 57.3 mm | -0.06 35.3 mm | -0.11 445 N |
| 5 | -0.30 6.9° | -0.21 7.6 mm | 0.62 57.7 mm | -0.47 34.3 mm | 0.07 540 N |
| 6 | -0.44 5.6° | -1 6 mm | 0.88 58.6 mm | -0.88 33.3 mm | 0.27 638 N |
| 7 | -0.53 4.7° | 1 10 mm | 0.41 56.9 mm | -1 33.0 mm | 0.33 669 N |

Several selection criteria can be considered to adopt a solution. Because of the precision of the models, it is decided here to select the optimal solution which is the closest to one of the tests of the realised experiment design.

According to this criterion the first solution of Table 6 is taken. This solution has been simulated. The results are shown in Table 7:

Table 7: Verification of the chosen optimal solution for stamping parameters

| No. | A' | R' | W' | D' | F' | $A1$ | $A2$ | H |
|-----|---------------|------------|--------------|------------|---------------|---------------------|--------|----------|
| 19 | 0.35 13.5° | -1 6 mm | 0.75 58.1 | 1 38 mm | -0.91 47 N | Theoretica: 135° | 135° | 30.44 mm |
| | | | | | | Realb: 133.8° | 134.5° | 30.4 mm |
| | | | | | | Deviationc: 1.2° | 0.5° | 0.4 mm |

a – obtained with the polynomial model.

b – obtained with the numerical simulation by FEM.

c – $(Y_{\text{theoretic}} - Y_{\text{real}})$.

The simulation of this solution gives the results very close to those predicted, particularly for A_2 and H .

4. Conclusion

A method of optimization of stamping processes with numerical simulations has been presented. It uses the fractional experiment designs to obtain linear relations between the geometrical parameters of the formed part and the parameters related to the process of stamping. Those relations allow one to determine the influence of the stamping parameters (tool geometry, blankholder force, punch velocity) on the part geometry [5] and to optimize their values.

Here, it has been applied to an example presenting an important springback and it enables one to determine the shape of the tool and the optimal stamping conditions to compensate for the effects of this springback on simulated parts.

If the results of the numerical simulation are close to reality, the stamping process so designed will give parts of the expected shape.

The models adopted here could be improved by conducting additional tests in order to take the non-linearity of the phenomena and the interactions between stamping parameters of the higher order into account.

This method, under development, will allow one to optimize the design of industrial stamping processes by limiting the expensive tests and the corrections in the press shop.

References

- [1] Zimniak Z.: *Tooling design for sheet metal forming processes compensating springback error*, Proceedings of the 6th ESAFORM Conference on Material Forming, V. Brucato (ed.), Italy, April 28–30, 2003.
- [2] Browne M.T., Hillery M.T.: *Optimising the variables when deep-drawing C.R.I cups*, Journal of Material Processing Technology, 2003, 136, pp. 64–71.
- [3] Colgan M., Monaghan J.: *Deep drawing process: analysis and experiment*, Journal of Material Processing Technology, 2003, 132, pp. 35–41.
- [4] Dumoulin S., Tabourot L., Chappuis C., Vacher P., Arrieux R.: *Determination of the equivalent stress-equivalent strain relation of a sample of copper in tensile loading*, International Journal of Material Processing Technology, 2003, 133, pp. 79–83.
- [5] Pairel E., Ledoux Y., Tabourot L., Arrieux R.: *A method to determine relations between process conditions and draw part geometry*, XVI International Scientific and Technological Conference on Design and Technology of Drawpieces and Die Stamping, June 14–16, 2004, Poznań, Poland.

Korekcja geometrycznych defektów wyrobów tłoczonych za pomocą symulacji numerycznej i planowania eksperymentu

Zaproponowano metodę korekcji i optymalizacji procesów tłoczenia. Aby określić sprężynowanie wyrobów charakteryzujących się dużymi odkształceniami, zastosowano sprzężoną metodę planowania eksperymentu i metodę elementów skończonych. Określono istotne parametry wpływające na sprężynowanie, a następnie zastosowano analizę czynnikową i odpowiednie symulacje numeryczne. Wyniki w postaci zdeformowanych siatek zostały użyte do określenia wirtualnej geometrii wyrobów. Określono zależności liniowe pomiędzy geometrią wyrobu i parametrami procesu, które umożliwiły ustalenie ich wpływu i wzajemnego oddziaływania na kształt geometryczny wyrobów. Te zależności pozwoliły ustalić poprawne wartości parametrów procesu umożliwiające otrzymanie wyrobów o oczekiwanej geometrii.



Information about PhD thesis at the Civil Engineering Faculty and the Mechanical Engineering Faculty of Wrocław University of Technology

Title: *Nondestructive identification of compression strength of concrete by means of neural networks (in Polish)*
Nieniszcząca identyfikacja wytrzymałości na ściskanie betonu z wykorzystaniem sztucznych sieci neuronowych

Author: Krzysztof Schabowicz

Supervisor: Doctor Jerzy Hoła, Professor of Wrocław University of Technology

Promoting Council: Institute of Civil Engineering, Wrocław University of Technology

Reviewers:

Professor Zenon Waszczyszyn

Professor Mieczysław Kamiński

Date of PhD thesis presentation: February 11th, 2003

PhD thesis is available in Main Library and Scientific Information Centre of WUT

The monograph contains: 181 pages, 63 figs, bibliography: 176 items

Keywords: *nondestructive tests, concrete, compression strength, artificial neural networks*

Abstract: Results of experimental and numerical analyses proving that artificial neural networks are suitable for identifying the compression strength of concrete on the basis of its parameters evaluated by nondestructive methods are presented. An overview of the literature on nondestructive methods of evaluating the compression strength of concrete is given. Compression strength identification techniques are compiled and analyzed. Also an overview of the literature on artificial neural network is presented. Neural networks most suitable for the task have been selected.

A database for seven concretes differing in their compression strength and type of aggregate was created on the basis of external and in-house research results. Thus patterns for teaching and testing the selected neural networks were established.

The artificial neural networks have proved to be suitable for identifying the compression strength of concrete. Novel methods of identifying the compression strength of concrete on the basis of its parameters evaluated by nondestructive techniques have been developed. The methods have been verified by applying them to real building structures.

Title: *Mechanism of strain fracture of materials in quasi-isothermal cutting with one-sided concentrator of stresses (in Polish)*
Mechanizm lokalizacji odkształceń i pękania materiałów przy quasi-izotermicznym ścinaniu z jednostronnym koncentratorem naprężeń

Author: Grzegorz Chruścielski

Supervisor: Professor Edward Stanisław Dzikowski

Promoting Council: Mechanical Faculty, Institute of Production Engineering and Automation, Wrocław University of Technology

Reviewers:

Professor Jerzy Gronostajski

Professor Józef Zasadziński

Date of PhD thesis presentation: September 30th, 2002

PhD thesis is available in Main Library and Scientific Information Centre of WUT

The monograph contains: 107 pages, 45 figs, bibliography: 165 items

Keywords: *chip formation model, mesomechanism, ductile fracture, low SFE materials*

Abstract: The process of cutting with one active concentrator of tensions is characterized by its periodicity which causes that the material being separated takes on the shape of chip. This does not occur when two active concentrators of tensions are used for cutting. As is well known, the type of chip results in waste of both energy and tools as well as reliability of machines, especially those being numerically controlled. Therefore, investigations of the mechanisms that determine the type of chip and choice of chip formation process modelling technique are the principle object of present dissertation.

For this reason, the analysis of current state of knowledge of one active concentrator of tension-based process modelling was carried out. It was affirmed that well-known models of continuous chip were not able to generate the criteria of fracture of cutting material and they cannot predict the other types of chips. It was assumed that the main cause of the above was lack of explicit conception of physical modelling of this group of processes. In particular, this concerns the cutting in isothermal conditions, where the most of well-known types of chips are formed, including continuous chip – the least desirable for automatic machining centres.

It was put forward a thesis that further development of modelling of the processes based on one active concentrator of tensions was possible only due to development of a new conception of physical modelling. In order to support this thesis, a mesoscope conception of modelling of two-concentrators-based processes reported by Dzikowski was applied. This conception is based on structural levels of plastic deformation, especially on the results of dislocation structure evolution leading to deformation localization in isothermal shear bands. Thus it generates new criteria and possibilities for controlling the fully comprehended processes of cutting.

It was proposed the experimentally verified new model of cutting with one active concentrator of tensions. This model is based on the conception of Dzikowski, but some modifications in specificity (cycle) of processes based on cutting with one active concentrator of stresses are made. Therefore, it can be applied to the description of mechanism and the way of forming different types of chips. In particular, this model is useful for modelling the processes based on separation of thin layers of material by plastic cutting.

Title: *Influence of slides on frictional contact in conditions of dry rolling-sliding friction (in Polish)*
Wpływ poślizgów na sprzężenie cierne w warunkach suchego tarcia toczno-ślizgowego

Author: Zbigniew Ferenc

Supervisor: Professor Czesław Koziarski

Promoting Council: Institute of Machines Design and Operation, Wrocław University of Technology

Reviewers:

Professor Włodzimierz Waligóra

Professor Zbigniew Lawrowski

Date of PhD thesis presentation: April 27th, 2004

PhD thesis is available in Main Library and Scientific Information Centre of WUT

The monograph contains: 128 pages, 104 figs, bibliography: 133 items

Keywords: *microslip, kinematic slip*

Abstract: The influence of tangent forces on overloads occurring on the contact surfaces of collaborating machine elements and torque transmission instability, deformation continuity and displacements associated with this were presented. The measurements of forces and torque coupled with friction at the strictly set slide values and revolving and linear speeds were carried out. Displacement on the contact surfaces was measured by optical method following completion of force and torque measurements. Temperature on anterior surface at a few chosen parameters of coupling was registered. At the end the results of investigation of cone-form metal samples seizing were presented. Temperature and resistant forces at 15% sliding were measured.

Title: *An influence of mechanical stabilisators on the changes in the spine flexibility (in Polish)*
Wpływ zastosowania stabilizatorów mechanicznych na zmiany podatności kręgosłupa

Author: Agnieszka Szust

Supervisor: Professor Romuald Będziński

Promoting Council: Institute of Machines Design and Operation, Wrocław University of Technology

Reviewers:

Professor Jan Marciniak

Doctor Mieczysław Szata

Date of PhD thesis presentation: November 19th, 2004

PhD thesis is available in Main Library and Scientific Information Centre of WUT

The monograph contains: 210 pages, 203 figs, bibliography: 112 items

Keywords: *biomechanics of the human spine, overstress, stability, method of the stabilisation*

Abstract: The monograph deals with the human spine, in particular it analyses of the load of the lumbar and thoracic spines in physiological conditions under functional load and in pathologically destabilised conditions. Experimental examination of the specimens of a natural lumbar spine was carried with the testing machine MTS-Bionix.

The examination consists of: a physiological spine test, a destabilized spine test; a test on a destabilized spine that was restabilized by the systems of implants used in orthopaedic treatment of lateral curvatures of the spine. The test carried out on three stabilizing systems made it possible to analyse the response of the lumbar and thoracic spines to flexion/extension and compression.

This experimental analysis is necessary for characterising the factors affecting the spine flexibility.

Title: *Wavelet analysis in parametric identification of discrete dynamic systems (in Polish)*
Analiza falkowa w parametrycznej identyfikacji dyskretnych układów dynamicznych

Author: Magdalena Napiórkowska-Alykow

Supervisor: Professor of Wrocław University of Technology Wojciech Głabisz

Promoting Council: Institute of Civil Engineering, Wrocław University of Technology

Reviewers:

Professor Jerzy Rakowski, Poznań University of Technology

Professor Paweł Śniady, Wrocław University of Technology

Date of PhD thesis presentation: October 20th, 2004

PhD thesis is available in Main Library and Scientific Information Centre of WUT

The monograph contains: 150 pages, 59 figs, bibliography: 146 items

Keywords: *wavelet packet analysis, parametric identification*

Abstract: The dissertation presents an application of, never used so far, wavelet packet analysis in the parametric identification of discrete dynamic systems. A new algorithm, founded on Walsh packet properties, was developed and applied in solving signal derivatives, which are the basis of the parametric identification of discrete dynamic systems. A new procedure of identification, based on the Haar filter and filtered form of signal derivatives, was developed. This procedure enables reduction of derivative degree. The algorithms were tested in single degree of freedom systems (SDOF) and two degree of freedom systems, which were described by linear and nonlinear equations with constant and variable coefficients.

Title: *Usefulness of polymer sulphur composites to the protection of reinforcement and concrete against corrosion (in Polish)*
Przydatność polimerowych kompozytów siarkowych do ochrony przed korozją stali zbrojeniowej i betonu

Author: Mariusz Książek

Supervisor: Professor of Wrocław University of Technology Jerzy Hoła

Promoting Council: Institute of Civil Engineering, Wrocław University of Technology

Reviewers:

Professor Lech Czarnecki

Professor Mieczysław Kamiński, Wrocław University of Technology

Date of PhD thesis presentation: June 16th, 2004

PhD thesis is available in Main Library and Scientific Information Centre of WUT

The monograph contains: 152 pages, 101 figs, bibliography: 137 items

Keywords: *polymer sulphur composite, surface protection against corrosion, reinforcement, concrete*

Abstract: This paper presents the results of the experimental research and analyses indicating the usefulness of polymer sulphur composites to the protection of reinforcement and concrete against corrosion. The paper presents the review of the literature, among other things, a select use of polymer sulphur composites in buildings, the methods of the surface protection of reinforcement and concrete against corrosion and the methods of evaluating a protection layer on these materials. The research deals with the composition of materials and the conditions for their formation. The physical and mechanical properties of polymer sulphur composites were evaluated. After the analysis of the initial results the optimum compositions of polymer composites were chosen. The experimental program comprised: adhesion of the composite to smooth and ribbed reinforcement and to a standard mortar and concrete, the loss of the composites or reinforcement and ordinary concrete in acid solutions, alkaline and salt solutions and in the water. Parallely the polarization tests were carried out on reinforcement and concrete with or without covering them with polymer sulphur composites. The usefulness of polymer sulphur composites to the surface protection of reinforcement and concrete against corrosion was evaluated.

Title: *Modelling and dynamic analysis of steel beam bridges under moving load (in Polish)*
Modelowanie i analiza dynamiczna belkowych mostów stalowych pod obciążeniem ruchomym

Author: Monika Podwórna

Supervisor: Professor Marian Kłasztorny

Promoting Council: Institute of Civil Engineering, Technical University of Wrocław

Reviewers:

Professor Paweł Śniady

Doctor Roman Lewandowski

Date of PhD thesis presentation: June 18th, 2003

PhD thesis is available in Main Library and Scientific Information Centre of WUT

The monograph contains: 137 pages, 53 figs, 18 tables, bibliography: 42 items

Keywords: *railway bridge, steel beam bridge, trains, non-linear modelling, dynamic analysis*

Abstract: The dissertation concerns dynamics of single-track, single-span, steel beam railway bridges carrying high-speed passenger trains. Physically non-linear modelling of the bridge-track-moving train system (MTP) and a computer algorithm for calculating dynamic and quasi-static responses of a bridge to a moving train are developed. The main goal is to derive a design model of the MTP system, i.e. the model with simplifications acceptable from a practical point of view. Dynamic analysis of steel beam bridges loaded with passenger trains moving at velocities of 100–300 km/h has been performed on a series-of-types of bridges.

Title: *Deflection of the continuous RC beams under sustained loads*
(in Polish)

Ugięcia długotrwanie obciążonych statycznie niewyznaczalnych belek żelbetowych

Author: Sebastian Toś

Supervisor: Professor of Wrocław University of Technology Mariusz Szechiński

Promoting Council: Institute of Civil Engineering, Wrocław University of Technology

Reviewers:

Professor Tadeusz Godycki-Ćwirko, Gdańsk University of Technology

Professor Mieczysław Kamiński, Wrocław University of Technology

Date of PhD thesis presentation: October 13th, 2004

PhD thesis is available in Main Library and Scientific Information Centre of WUT

The monograph contains: 134 pages, 187 figs, bibliography: 119 items

Keywords: *reinforced concrete, continuous beams, long-term deflection*

Abstract: The dissertation deals with the behaviour of the continuous RC beams under sustained loads. Two-span beams of rectangular and T-shaped cross sections were analyzed. The tests were conducted on elements in the uncracked phase and in the phase after cracking.

In order to find the load-carrying capacity of the elements, a disruptive investigation was carried out. Besides the author evaluated the material characteristics of the concrete and the steel: compressive and tensile strength as well as the modulus of elasticity. Simultaneously the rheological behaviour of the concrete used (creep and shrinkage) under the sustained loads was investigated. The concrete samples in the shape of a cylinder were used. The results were given in the form of diagrams and represented by mathematical functions as well.

In theoretical research, the author analyzed present methods of estimating the deflections of RC structures under sustained loads. He assumed that it was possible to estimate the deflection of the RC structure under sustained load by reducing its stiffness in time. The effects of theoretical analysis were compared with experimental results.

Title: *The influence of subsoil vibrations on horizontal pressure of granular material exerted on silo walls (in Polish)*
Wpływ drgań podłoża gruntowego na poziome parcia materiału sypkiego na ściany silosu

Author: Radosław Tatko

Supervisor: Professor of Wrocław University of Technology Sylwester Kobiela

Promoting Council: Institute of Civil Engineering, Wrocław University of Technology

Reviewers:

Professor Roman Ciesielski, Cracow University of Technology

Professor Mieczysław Kamiński, Wrocław University of Technology

Date of PhD thesis presentation: June 9th, 2004

PhD thesis is available in Main Library and Scientific Information Centre of WUT

The monograph contains: 133 pages, 163 figs, bibliography: 66 items

Keywords: *silo, granular material, subsoil vibrations, horizontal pressure*

Abstract: The dissertation describes laboratory investigation of steel flat-bottomed silo model filled with sand and subjected to external dynamic loads. The silo was placed on a system of springs, which represents a subsoil. The loads in the form of horizontal impulses were applied to a bottom plate of the silo. Horizontal pressure in time was used for analysing the influence of subsoil vibrations on the distribution of the pressure changes. Basic conclusions: (1) the subsoil vibrations cause two types of changes of the horizontal pressures: constant changes which are observed after completion of model vibrations and cyclic momentary changes; (2) the subsoil vibrations generate a constant increase or constant decrease in pressure.

Title: *Application of wavelets in direct methods of structural mechanics*
(in Polish)
Zastosowanie falek w przybliżonych metodach mechaniki budowli

Author: Tomasz Koźbial

Supervisor: Doctor Wojciech Glabisz, Professor of Wrocław University of Technology

Promoting Council: Institute of Civil Engineering, Wrocław University of Technology

Reviewers:

Doktor Jerzy Rakowski, Professor of Poznań University of Technology

Professor Piotr Konderla

Date of PhD thesis presentation: May 12th, 2004

PhD thesis is available in Main Library and Scientific Information Centre of WUT

The monograph contains: 91 pages, 46 figs, 9 tables, bibliography: 87 items

Keywords: *wavelet analysis, direct methods*

Abstract: The dissertation presents a new, rarely used so far, way of constructing the solutions in the direct methods of structural mechanics which involves wavelet approximations. Discrete and wavelet packet analyses are used in some one- and two-dimensional boundary-value problems analysed by the extended Galerkin and Ritz methods. New adequate algorithms are developed and applied in solving mechanical problems such as bending of beams and plates and stability analysis of beams. The results obtained are compared with the exact solutions or with those from the traditional finite-element method. The techniques of computation of integrals of the products of wavelets and their derivatives (called *connection coefficients*) for Daubechies wavelet family are proposed.